Journal of Pharmacokinetics and Pharmacodynamics (2019) 46:319–338
https://doi.org/10.1007/s10928-019-09641-8

ORIGINAL PAPER

A translational platform PBPK model for antibody disposition in the brain

Hsueh-Yuan Chang[1] · Shengjia Wu[1] · Guy Meno-Tetang[2] · Dhaval K. Shah[1]

Received: 1 January 2019 / Accepted: 6 May 2019 / Published online: 21 May 2019

Abstract

In this manuscript, we have presented the development of a novel platform physiologically-based pharmacokinetic (PBPK) model to characterize brain disposition of mAbs in the mouse, rat, monkey and human. The model accounts for known anatomy and physiology of the brain, including the presence of distinct blood–brain barrier and blood–cerebrospinal fluid (CSF) barrier. CSF and interstitial fluid turnover, and FcRn mediated transport of mAbs are accounted for. The model was first used to characterize published and in-house pharmacokinetic (PK) data on the disposition of mAbs in rat brain, including the data on PK of mAb in different regions of brain determined using microdialysis. Majority of model parameters were fixed based on literature reported values, and only 3 parameters were estimated using rat data. The rat PBPK model was translated to mouse, monkey, and human, simply by changing the values of physiological parameters corresponding to each species. The translated PBPK models were validated by a priori predicting brain PK of mAbs in all three species, and comparing predicted exposures with observed data. The platform PBPK model was able to a priori predict all the validation PK profiles reasonably well (within threefold), without estimating any parameters. As such, the platform PBPK model presented here provides an unprecedented quantitative tool for prediction of mAb PK at the site-of-action in the brain, and preclinical-to-clinical translation of mAbs being developed against central nervous system (CNS) disorders. The proposed model can be further expanded to account for target engagement, disease pathophysiology, and novel mechanisms, to support discovery and development of novel CNS targeting mAbs.

Keywords Brain · Monoclonal antibody · Pharmacokinetics · PBPK model · Interspecies scaling · Blood–brain barrier · Blood–CSF barrier

Introduction

Drug development scientists have spent significant amount of time and resources to develop monoclonal antibodies (mAbs) against central nervous system (CNS) disorders (Supplementary Table 1). However, to date there is not a single clinically approved antibody that works in brain parenchyma [1, 2]. One of the reasons behind these clinical failures could be our limited understanding of mAb disposition at the sites-of-action in the brain [1, 3]. In fact, there are only limited methodologies available to measure brain exposure of mAb in the clinic. While brain biopsy and microdialysis may be performed under critical conditions [4, 5], typically cerebrospinal fluid (CSF) collected from the lumbar spine (LS) is used to measure brain exposure of antibody in the clinic [6–9]. However, most of the CSF is produced at the choroid plexus epithelium cells, and hence CSF concentrations of mAb is a measure of

Electronic supplementary material The online version of this article (https://doi.org/10.1007/s10928-019-09641-8) contains supplementary material, which is available to authorized users.

✉ Dhaval K. Shah
dshah4@buffalo.edu

[1] Department of Pharmaceutical Sciences, School of Pharmacy and Pharmaceutical Sciences, The State University of New York at Buffalo, 455 Kapoor Hall, Buffalo, NY 14214-8033, USA

[2] Quantitative Clinical Pharmacology/PK-PD, Modeling & Simulation, Immunology/Inflammation, UCB Pharmaceuticals, Brussels, Belgium

mAb transport across blood–CSF barrier (BCSFB) and do not represent the delivery of mAb across blood–brain barrier (BBB) endothelial cells [1]. Thus, CSF concentrations of mAb are more closely associated with mAb exposure at the ependymal surface of the brain and spinal cord, and may not accurately represent mAb exposure at parenchyma or the site-of-action [10–12]. Preclinically, mAb concentrations in brain homogenate is routinely used as a surrogate for concentrations at the site-of-action. However, the pharmacokinetics (PK) of mAb in different regions of the brain (including the site-of-action) can be very different [10–13], and the use of brain homogenate concentrations can hamper the development of a robust and translational exposure–response relationship for mAbs. Consequently, there is a need for novel methods that can accurately predict the concentrations of mAb at the site-of-action in the brain.

One such method can be development of mathematical models that can predict the PK of mAbs in the brain. In fact, there are a couple of PK models already published that attempt to predict the disposition of mAb in mice and monkey brain [14, 15]. However, these models are empirical in nature and only predict whole brain PK of mAb. As such, they are not capable of distinguishing between mAb exposure in different regions of the brain, and accounting for preferential distribution of mAb in certain regions of the brain (e.g. anti-TfR mAb accumulation in brain endothelium) [16–20]. In addition, since these models are not physiological, their ability to translate preclinical data to the clinic and predict the PK of mAb in different regions of human brain remains limited. In fact, these models have not been validated using clinical data yet. Consequently, there is a need to develop more mechanistic models like physiologically-based pharmacokinetic (PBPK) model, which can predict the exposure of mAb in different regions of brain and facilitate preclinical-to-clinical translation of mAbs.

PBPK models have been extensively used to characterize plasma and tissue PK of mAbs in preclinical species and humans [21–29]. They incorporate anatomical and physiological factors to describe mAb biodistribution, and provide a platform for clinical translation of mAbs. Since PBPK models can incorporate mAb-neonatal FcR (FcRn) interaction, mAb-target interaction, target biology, and disease pathology, they can allow prediction of first-in-human starting dose and determination of clinically efficacious dosing regimen. However, all the mAb PBPK models published so far either omits the brain tissue [21–25, 29] or assumes it to be similar to other peripheral tissues [26–28]. To date, there has been no published mAb PBPK model that accounts for unique anatomy and physiology of brain. As such, there is a need for more physiological brain PBPK models that can account for differential entry of mAb across BBB and BCSFB, and unique disposition of mAb in different regions of the brain [13]. These models can not only help in establishing a quantitative relationship between concentrations of mAb in different regions of the brain, but can also provide a quantitative platform for preclinical-to-clinical translation of CNS targeting mAbs. In this manuscript, we have presented the development of one such PBPK model.

The platform PBPK model presented here accounts for many known physiological processes responsible for the disposition of non-targeting mAbs in the brain, including CSF circulation, complex movement of macromolecules within the CNS [30–32], and FcRn mediated mAb disposition [33–37]. The model was developed using published and in-house PK data on mAb disposition in rat brain. This dataset included the PK of non-targeting mAb and endogenous IgG in brain homogenate, and the PK in brain interstitial fluid (ISF) at the striatum (ISF_{ST}), CSF at the lateral ventricles (CSF_{LV}), and CSF at the cisterna magna (CSF_{CM}), determined using our recently published state-of-the-art microdialysis method [13]. The model was validated using published PK data on mAb disposition in mouse, monkey, and human brain.

Methods

Datasets for modeling

MAb PK data for building and validating the brain PBPK model were obtained from literature or in-house experiments as shown in Table 1. To avoid the complexity of target-mediated disposition or other enhanced brain delivery mechanisms, only non-targeting IgG and endogenous IgG profiles were selected. All published datasets were digitized using a free online tool (https://automeris.io/WebPlotDigitizer/), and only mean data were used for the analysis.

Data for development of rat PBPK model

Rat PK data were used for the development of the platform PBPK model, and the data from other species were used for validation purpose. PK of a non-cross reactive exogenous immunoglobulin G (IgG) and endogenous IgG in plasma and different regions of rat brain was obtained from our previously published microdialysis investigation [13]. This study analyzed the PK of trastuzumab (a control human IgG1) in rat plasma, brain homogenate, striatum (ISF_{ST}), lateral ventricle (CSF_{LV}), and cisterna magna (CSF_{CM}), after intravenous administration of 10 mg/kg dose. Concentrations of rat endogenous IgG were also measured in the same compartments. Of note, the brain tissue was

Table 1 Datasets used to build the model

Species	Antibody	Administration	Dose	References
Mouse	Non-specific mouse IgG1, 7E3	IV	8 mg/kg	[34]
	Anti-gD mAb	IV	100 mg/kg	[41]
Rat	Trastuzumab	IV	10 mg/kg	[13]
	Endogenous IgG	–	–	[13]
	FcRn-nonbinding Trastuzumab	IV	10 mg/kg	In house data
	Anti-JC virus mAb (399 H0/L0)	IV	10 mg/kg	[38]
	Tocilizumab	ICV	0.5 mg/kg	[39]
	Anti-ganglioside GD2 IgG3, 3FB	Intrathecal administration	1 mg/kg	[40]
Monkey	Trastuzumab	Intrathecal administration	0.24 mg/g brain/week	[42]
	Anti-gD mAb	ICV infusion	1.68 mg/kg/h	[12]
	Anti-α-synuclein mAb, BIIB054	IV	100 mg/kg	[38]
Human	Endogenous IgG1 and IgG4	–	–	[43]
	IgG4 mAb, GNbAC1	IV	6,18,36 mg/kg	[44]

IgG Immunoglobulin G, *mAb* monoclonal antibody, *IV* intravenous administration, *ICV* Intracerebroventricular administration

collected following perfusion. In order to gain more insight into the role of FcRn in brain disposition of mAbs, in-house PK data obtained using FcRn nonbinding trastuzumab (I253A/H310A/H435A mutation) were used. The PK of FcRn nonbinding trastuzumab in rat brain was obtained using the same study design that is detailed above for trastuzumab. In order to include published data on brain PK of other mAbs in rat, plasma and CSF PK of another mAb were obtained from Wang et al. [38]. They analyzed CSF_{CM} PK of an anti-JC virus mAb (399 H0/L0), which has no binding in rat, following intravenous administration of 10 mg/kg dose. In order to include mAb PK data obtained following administration mAb by other routes, and to get more granularity on distribution of mAb from LV to CM, CSF PK data obtained by Noguchi et al. were used [39]. They analyzed the PK of a non-specific human IgG1, tocilizumab, in CSF_{CM} and plasma after intracerebroventricular (ICV) administration of 0.5 mg/kg dose. In order to characterize mAb clearance from CSF, another PK data obtained from Bergman et al. was included [40]. They analyzed the PK of a murine anti-ganglioside GD2 IgG3, 3F8, in CSF obtained from the LS after Intrathecal administration of 1 mg/kg dose.

Data for validation of mouse PBPK model

In order to validate the mouse model, plasma and brain PK of mAb in wild-type mice were obtained from Garg and Balthasar [34]. They analyzed the PK of a non-specific mouse IgG1 antibody, 7E3, in plasma and brain after intravenous administration of 8 mg/kg dose. While the brain samples collected in this study were not perfused, the amount of antibody in the brain was corrected for the residual blood volume obtained using ^{51}Cr-labeled red blood cells (RBCs). Another mouse plasma and brain PK data at higher mAb dose were obtained from Atwal et al. [41]. They analyzed the PK of a non-specific IgG1, anti-gD, in plasma and perfused brain after single and multiple *i.v.* administrations of 100 mg/kg dose.

Data for validation of monkey PBPK model

In order to validate the monkey model, serum and CSF PK of mAb in monkey were obtained from Braen et al. [42]. They analyzed the PK of trastuzumab in monkey serum and CSF after intrathecal injection of 15 mg dose once a week (i.e. 0.24 mg/g brain, weekly). CSF samples in this study were collected via a catheter placed in the CM. Additional data on serum and CSF PK of mAb in monkey were obtained from Yadav et al. [12]. They analyzed a non-specific mAb, anti-gD, in serum and CSF of monkey after ICV infusion of 1.68 mg/kg/h over 6 weeks. Another dataset for plasma and CSF PK of mAb in monkey were obtained from Wang et al. [38]. They analyzed plasma and CSF PK of anti-aggregated α-synuclein mAb, BIIB054, in healthy monkey after *i.v.* administration of 100 mg/kg dose.

Data for validation of human PBPK model

In order to validate the human model, endogenous concentrations of human IgG1 and IgG4 in lumbar CSF (CSF_{LS}) were obtained from Kaschka et al. [43]. Model predicted CSF/plasma ratio of mAb at steady-state was compared with the clinically reported values for the endogenous antibodies. Plasma and CSF PK of

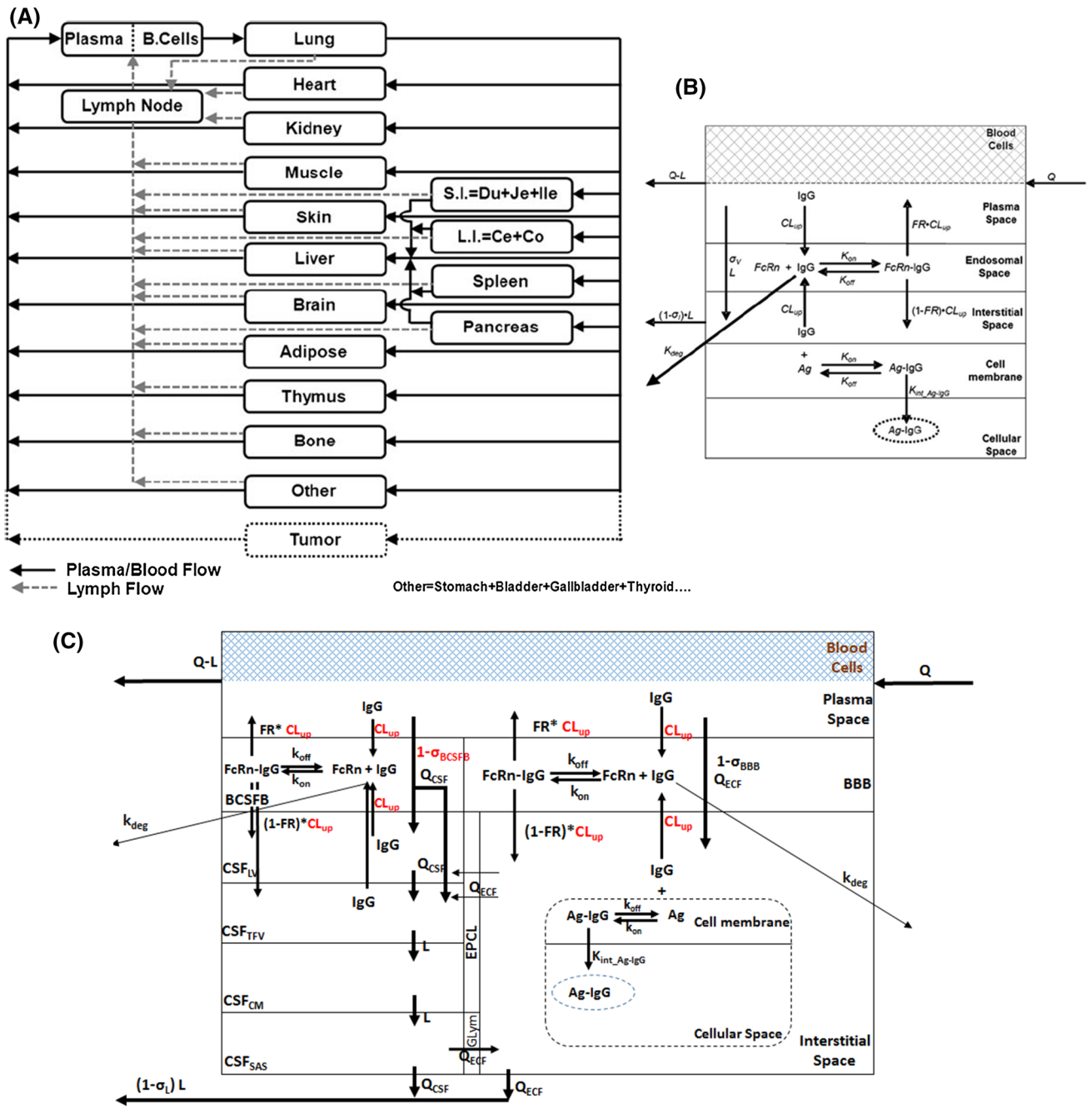

Fig. 1 Structure of the whole-body and platform brain PBPK model for mAb disposition. **a** Schematic of the whole-body PBPK model. All organs are connected in an anatomical manner using blood flow (solid arrows) and lymphatic flow (dashed arrows) (please refer to [27] for more details). **b** Schematic of a typical tissue compartment within the PBPK model (please refer to [27] for more details). **c** Schematic of the brain PBPK model. The brain compartment is divided into brain parenchymal compartment and CSF compartments. For detailed description of the symbols and drug disposition process, please refer to the *model structure* section in the *methods* section

exogenously administered mAb in human were obtained from Curtin et al. [44]. In a Phase-I study, the authors analyzed plasma and CSF PK of a humanized IgG4 monoclonal antibody, GNbAC1, in healthy individuals. The subjects received single intravenous infusion of 6, 18, 36 mg/kg dose, and the CSF_{LS} samples were collected using lumbar puncture.

Model structure

Schematic diagram of the proposed brain PBPK model is shown in Fig. 1. The brain PBPK model is integrated into the platform PBPK model for mAbs published before [27]. The complete PBPK model includes 16 tissue compartments (blood, lung, heart, kidney, muscle, skin, liver,

adipose, thymus, bone, small intestine, large intestine, spleen, pancreas, other/carcass, and brain) and a lymph node compartment, connected to each other in an anatomical manner using blood and lymph flow (Fig. 1a).

Each tissue compartment, except brain, is composed of vascular, endosomal, interstitial, and cellular sub-compartments (Fig. 1b). The vascular sub-compartment contains plasma and blood cell compartments. MAb is assumed to enter tissue vascular compartment via arterial blood flow (Q_p^i) and exit via venous blood flow, which is represented as arterial blood flow subtracted by the lymphatic flow ($Q_p^i - L^i$). MAb is assumed to travel from plasma to interstitial space via paracellular pores, using convective lymph flow (L^i) with the resistance described by vascular reflection coefficient (σ_V^i), or via pinocytosis (CL_{up}^i) and FcRn mediated transcytosis across vascular endothelial cells.

It is well-known that FcRn protects serum IgG from catabolism, and this protein is expressed in variety of tissues and cell types, including endothelial cells [45], keratinocytes [46], hepatocytes [47], mammary epithelium [48], and bone marrow derived phagocytic cells [49]. In addition, bone marrow derived cells have shown significance in extending the half-life of serum IgG during preclinical investigations [49]. However, due to lack of quantitative and reliable information about the expression of FcRn in all these tissues from different species, in our previously published platform PBPK model we assumed that the site where FcRn is protecting IgG from catabolism exist mainly within the vascular endothelial cells. We also assumed that FcRn concentrations in the vascular endosomal space are conserved among different tissues and between different species. These assumptions led to a single estimated value of FcRn concentrations (4.982E−05 M), which was similar to the value reported by Ferl et al. (4.00E−05 M) for mouse [24] and Garg and Balthasar (3.30E−05 M) for human [50].

MAb molecules in the endosomal space of endothelial cells are assumed to interact with FcRn using association (k_{on}) and dissociation (k_{off}) rate constants. FcRn bound mAb molecules are assumed to recycle to either plasma space (using fraction recycled to plasma space, *FR*) or to the interstitial space (using *1-FR*). Unbound mAb molecules in the endosomal space are assumed to degrade via a first order degradation rate constant (k_{deg}). It is assumed that endothelial cells can also uptake the mAb molecules from the interstitial space. MAb molecules in the Interstitial space are assumed to exit the tissue compartment via convective lymph flow (L^i) with the resistance described by interstitial reflection coefficient (σ_L^i). The cellular membrane and cellular space in Fig. 1b can be used in the future to characterize cellular disposition of targeting mAbs. To characterize PK of non-targeting mAbs, these two compartments are not currently active in our model.

While the model structure of all tissues is kept the same as before, the augmented brain compartment is divided into two separate sub-compartments: CSF circulation system and brain parenchyma. Once in the brain vascular space, mAb is assumed to enter the brain via bulk flow through BBB or BCSFB. This bulk flow is responsible for the formation of CSF and ISF. Two reflection coefficients (σ_V^{BBB} and σ_V^{BCSFB}) were chosen to account for limited paracellular transport of mAbs across the two barriers. When σ_V^{BBB} or σ_V^{BCSFB} equals 1, the entry of mAb through paracellular pathway is completely shut down. Considering the difference in the tightness between BCSFB and BBB [1, 51], we assumed that there is no paracellular transport of IgG across BBB, and σ_V^{BBB} was assumed to be 1. The leakiness of BCSFB was estimated by the parameter σ_V^{BCSFB} using the data. It was assumed that the endosomal space of BBB and BCSFB could allow non-specific pinocytosis (CL_{up}^{brain}) and transcytosis of mAb across the barriers, which may result in a slow entry of IgG into brain parenchyma and CSF [52]. FcRn mediated efflux, recycling, and transcytosis of mAb across BBB and BCSFB was also incorporated into the brain capillary endosomal spaces. It was also assumed that free mAb molecules in the endosomal space can either bind to free FcRn or travel to lysosomal space for degradation. FcRn bound mAb molecules in the endosomal space were assumed to either recycle back to the plasma space or to the interstitial/CSF space. The fraction of FcRn bound mAb molecules that recycle to the plasma space (*FR*) is higher than 0.5 (0.715 to be exact) [53], which leads to preferential efflux of FcRn bound mAb molecules towards the plasma space. Since it is reported that FcRn is expressed in both brain endothelium cells and choroid plexus epithelium cells [35], but the difference in the level of expression between these cell types is not known, here we have assumed that both cell types have the same concentration of FcRn in the endosomal space (Table 2) [27].

CSF circulation in the brain was incorporated using the state-of-the-art information published on the subject matter [30–32, 51]. Choroid plexus was assumed to secret CSF into both lateral ventricles (LV) and third-forth ventricle (TFV). The formation of CSF from choroid plexus was divided into LV and TFV based on the volume ratio of these ventricles (e.g. 1:1 in rats). In addition, 10% of CSF was assumed to produce from brain ISF at the brain ependymal cellular layer (EPCL) [54]. This brain extracellular flow was also divided between LV and TFV. Cisterna magna (CM) and subarachnoid space (SAS) do not have choroid plexus that secretes CSF, and SAS is considered as a clearance site for CSF. A small portion of

Table 2 Values of physiological parameters for different species used to build the platform brain PBPK model for mAbs

Parameter	Mice value	Rat value	Monkey value	Human value
CSF volume (mL)	0.035 [1] 0.04 [75]	0.25 [76]	13 [1]	100 [1] 150 [76] 160 [88] 150–160 [89]
Q_{CSF}^{brain} CSF production (mL/h)	0.0192 [1] 0.0198 [78]	0.132 [76]	2.46 [1]	21 [1][76] 24 [81] 24–36 [80]
CSF turnover (times/day)	13.333 [1]	11 [76]	4.615 [1]	4[76] 5 [1]
Cerebral ISF volume (mL)	–	0.29 [76]	–	240 [76] 240–280 [80]
Q_{ECF}^{brain} Cerebral ISF production (mL/h)	0.00192[b]	0.012–0.03 [76] [79] 0.012 [81] 0.0216 [82] 0.02–0.31 [83]	1.23[c]	9–12 [76] 10.5 [81]
Brain total volume (mL)	0.485 [27] 0.303 [84]	2.28 [27] 1.88 [85]	94.0 [27]	1450 [27] 1400 [79]
V_{plasma}^{brain} Cerebral plasma volume (mL)	0.0107 [27]	0.0502 [27] 0.06 [85]	2.07 [27]	31.9 [27]
$V_{bloodcells}^{brain}$ Cerebral blood cell volume (mL)	0.00873 [27]	0.0410 [27]	1.69 [27]	26.1 [27]
$V_{interstital}^{brain}$ Cerebral interstitial volume (mL)	0.0873 [27]	0.410 [27] 0.29 [81]	16.9 [27]	261 [27] 240 [81]
$V_{endosomal}^{brain}$ Cerebral endosomal volume (mL)	0.00243 [27]	0.0114 [27]	0.470 [27]	7.25 [27]
V_{cell}^{brain} Cerebral cellular volume (mL)	0.376 [27]	1.77 [27] 1.44 [81]	72.9 [27]	1124 [27] 960 [81]
V_{LV}^{brain} Lateral ventricle volume (mL)	0.0039–0.0041 [86]	0.05 [81]	1.463[e]	22.5 [81]
V_{TFV}^{brain} Third-Forth ventricle volume (mL)	0.0024–0.0025 [86]	0.05 [81]	1.463[e]	22.5 [81]
V_{CM}^{brain} Cisterna magna volume (mL)	0.0011[d]	0.017 [81]	0.488[e]	7.5 [81]
V_{SAS}^{brain} Subarachnoid space volume (mL)	0.0117[d]	0.18 [81]	5.85[e]	90 [81] 90–125 [79]
Surface area (meters^2)				
Blood–brain barrier		0.0140 [77] 0.0155 [87] 0.0263 [85]		17 [1] 12–18 [79]
Choroid plexus		0.0025 [87]		1.7 [1] 6–9 [79]
$\frac{SA_{BBB}}{SA_{BCSFB}}$ BBB to CP SA ratio	6.2[f]	6.2 [88] 10.12 [85]	10[f]	10 [1]
Brain weight (g)	0.3	1.8 [76]		1400 [1][1]
Q_{plasma}^{brain} Cerebral blood flow (mL/h)	11.8 [27]	65.3 [27] 66 [76]	1508 [27]	21453 [27] 42000 [76] 63000 [1] 36,600–51600 [79]
Choroid plexus blood flow (mL/h)				480 [1][1][a]
Q_{blood}^{brain} Blood cell flow (mL/h)	9.64 [27]	53.5 [27]	1234 [27]	17553 [27]

[a]Blood flow based on 4 mL/min/g for choroid plexus and 0.75 mL/min/g for brain [1]

[b]Assumes the brain ISF production rate is 10% of CSF formation rate in rodents [54]

[c]Assumes the brain ISF production rate is a fraction of CSF formation rate in monkey and human

[d]Assumes the ratio of V_{CM}^{brain} / V_{SAS}^{brain} is a constant in mice and rat and calculates mouse V_{SAS}^{brain} using the following equation: mouse = V_{SAS}^{brain}rat V_{SAS}^{brain} /(rat + V_{TFV}^{brain}rat V_{LV}^{brain})* (mouse + V_{TFV}^{brain}mouse V_{LV}^{brain})

[e]Assumes the ratio of the ventricle volume to brain total volume is a constant in monkey and human

[f]Assumes the SA ratio is constant in rodents, and the SA ratio is a constant in monkey and human

Underlined parameter values were used in the PBPK model

BBB blood–brain barrier, *CP* choroid plexus, *SA* surface area

CSF from SAS is reported to be reabsorbed via arachnoid villa. However, we did not include this pathway in the model, due to controversial findings about the existence of this CSF reabsorption pathway under normal CSF pressure. A portion of CSF from SAS may also go to brain parenchyma via perivascular space as glymphatic flow, which eventually enters the lymphatic system. Intracisternal administration of mAbs has confirmed the existence of this pathway [55]. However, due to the lack of physiological measurements and experimental data related to this pathway, here we have assumed clearance of mAb via this pathway is equal to CSF flow rate, which was multiplied by the lymph reflection coefficient σ_L.

Model equations

Our platform brain PBPK model is an augmented version of previously published platform PBPK model for mAbs [27]. Below are the equations for this model. Please refer to the glossary in the "Appendix" section for detailed description and units of the symbols used in the following equations. The initial condition for all the compartments is 0, except for $FcRn_{free}$ (4.982×10^{-5} M) and the compartment receiving the administered drug.

Blood compartment

Plasma

$$\begin{aligned} V_p \cdot \frac{dC^p}{dt} = & -\left(Q_p^{lung} + L^{lung}\right) \cdot C^p + \left(Q_p^{heart} - L^{heart}\right) \\ & \cdot C_p^{heart} + \left(Q_{plasma}^{kidney} - L^{kidney}\right) \cdot C_p^{kidney} \\ & + \left(Q_p^{brain} - L^{brain}\right) \cdot C_p^{brain} \\ & + \left(Q_p^{muscle} - L^{muscle}\right) \cdot C_p^{muscle} \\ & + \left(Q_p^{marrow} - L^{marrow}\right) \cdot C_p^{marrow} \\ & + \left(Q_p^{thymus} - L^{thymus}\right) \cdot C_p^{thymus} \\ & + \left(Q_p^{skin} - L^{skin}\right) \cdot C_p^{skin} + \left(Q_p^{fat} - L^{fat}\right) \cdot C_p^{fat} \\ & + \left(\left(Q_p^{SI} - L^{SI}\right) + \left(Q_p^{LI} - L^{LI}\right)\right. \\ & + \left(Q_p^{spleen} - L^{spleen}\right) + \left(Q_p^{pancreas} - L^{pancrease}\right) \\ & + \left.\left(Q_p^{liver} - L^{liver}\right)\right) \cdot C_p^{liver} + \left(Q_p^{other} - L^{other}\right) \\ & \cdot C_p^{other} + L^{LN} \cdot C^{LN} \end{aligned} \tag{1}$$

Note : $L^{brain} = Q_{CSF}^{brain} + Q_{ISF}^{brain}$

Note : $L^{LN} = Q_p^{lung} \cdot C\_LNLF$

Blood cells

$$\begin{aligned} V_{BC} \cdot \frac{dC^{BC}}{dt} = & -Q_{BC}^{lung} \cdot C^{BC} + Q_{BC}^{heart} \cdot C_{BC}^{heart} + Q_{BC}^{kidney} \\ & \cdot C_{BC}^{kidney} + Q_{BC}^{brain} \cdot C_{BC}^{brain} + Q_{BC}^{muscle} \cdot C_{BC}^{muscle} \\ & + Q_{BC}^{marrow} \cdot C_{BC}^{marrow} + Q_{BC}^{thymus} \cdot C_{BC}^{thymus} \\ & + Q_{BC}^{skin} \cdot C_{BC}^{skin} + Q_{BC}^{fat} \cdot C_{BC}^{fat} + (Q_{BC}^{SI} + Q_{BC}^{LI} \\ & + Q_{BC}^{spleen} + Q_{BC}^{pancreas} + Q_{BC}^{liver}) \cdot C_{BC}^{liver} \\ & + Q_{BC}^{other} \cdot C_{BC}^{other} \end{aligned} \tag{2}$$

Lymph node

$$\begin{aligned} V_{lymphnode} \cdot \frac{dC^{LN}}{dt} = & \left(1 - \sigma_L^{lung}\right) \cdot L^{lung} \cdot C_{IS}^{lung} \\ & + \left(1 - \sigma_L^{heart}\right) \cdot L^{heart} \cdot C_{IS}^{heart} \\ & + \left(1 - \sigma_L^{kidney}\right) \cdot L^{kidney} \cdot C_{IS}^{kidney} \\ & + \left(1 - \sigma_L^{SAS}\right) \cdot Q_{CSF}^{brain} \cdot C_{SAS}^{brain} \\ & + \left(1 - \sigma_L^{brainISF}\right) \cdot Q_{ECF}^{brain} \cdot C_{IS}^{brain} \\ & + \left(1 - \sigma_L^{muscle}\right) \cdot L^{muscle} \cdot C_{IS}^{muscle} \\ & + \left(1 - \sigma_L^{marrow}\right) \cdot L^{marrow} \cdot C_{IS}^{marrow} \\ & + \left(1 - \sigma_L^{thymus}\right) \cdot L^{thymus} \cdot C_{IS}^{thymus} \\ & + \left(1 - \sigma_L^{skin}\right) \cdot L^{skin} \cdot C_{IS}^{skin} + \left(1 - \sigma_L^{fat}\right) \\ & \cdot L^{fat} \cdot C_{IS}^{fat} + \left(1 - \sigma_L^{SI}\right) \cdot L^{SI} \cdot C_{IS}^{SI} \\ & \cdot \left(1 - \sigma_L^{LI}\right) \cdot L^{LI} \cdot C_{IS}^{LI} + \left(1 - \sigma_L^{spleen}\right) \\ & \cdot L^{spleen} \cdot C_{IS}^{spleen} + \left(1 - \sigma_L^{pancreas}\right) \\ & \cdot L^{pancreas} \cdot C_{IS}^{pancreas} + \left(1 - \sigma_L^{liver}\right) \\ & \cdot L^{liver} \cdot C_{IS}^{liver} + \left(1 - \sigma_L^{other}\right) \cdot L^{other} \\ & \cdot C_{IS}^{other} - L^{LN} \cdot C^{LN} \end{aligned} \tag{3}$$

Brain

Plasma compartment

$$\begin{aligned} V_p^{brain} \cdot \frac{dC_p^{brain}}{dt} = & \left(Q_p^{brain} \cdot C_p^{lung}\right) - \left(Q_p^{brain} - L^{brain}\right) \\ & \cdot C_p^{brain} - \left(1 - \sigma_V^{BBB}\right) \cdot Q_{ISF}^{brain} \cdot C_p^{brain} \\ & - \left(1 - \sigma_V^{BCSFB}\right) \cdot Q_{CSF}^{brain} \cdot C_p^{brain} - CL_{up}^{brain} \\ & \cdot V_{ES}^{brain} \cdot C_p^{brain} + CL_{up}^{brain} \cdot f_{BBB} \cdot V_{ES}^{brain} \\ & \cdot FR \cdot C_{BBB_{bound}}^{brain} + CL_{up}^{brain} \cdot (1 - f_{BBB}) \\ & \cdot V_{ES}^{brain} \cdot FR \cdot C_{BCSFB_{bound}}^{brain} \end{aligned} \tag{4}$$

$$f_{BBB} = \frac{SA_{BBB}}{SA_{BBB} + SA_{BCSFB}}$$

Unbound mAb in endosomal compartment at the brain–blood barrier (BBB)

$$\begin{aligned} V_{BBB}^{brain} \cdot \frac{dC_{BBB_{unbound}}^{brain}}{dt} = & CL_{up}^{brain} \cdot f_{BBB} \cdot V_{ES}^{brain} \\ & \cdot \left(C_p^{brain} + C_{IS}^{brain}\right) - V_{BBB}^{brain} \cdot k_{on}^{FcRn} \\ & \cdot C_{BBB_{unbound}}^{brain} \cdot FcRn_{free}^{BBB} + V_{BBB}^{brain} \cdot k_{off}^{FcRn} \\ & \cdot C_{BBB_{bound}}^{brain} - V_{BBB}^{brain} \cdot k_{deg} \cdot C_{BBB_{unbound}}^{brain} \end{aligned} \tag{5}$$

Bound mAb in endosomal compartment at the brain–blood barrier (BBB)

$$V_{BBB}^{brain}\cdot\frac{dC_{BBB_{bound}}^{brain}}{dt}=-CL_{up}^{brain}\cdot f_{BBB}\cdot V_{ES}^{brain}\cdot C_{BBB_{bound}}^{brain}+V_{BBB}^{brain}\cdot k_{on}^{FcRn}\cdot C_{BBB_{unbound}}^{brain}\cdot FcRn_{free}^{BBB}-V_{BBB}^{brain}\cdot k_{off}^{FcRn}\cdot C_{BBB_{bound}}^{brain} \tag{6}$$

Unbound mAb in brain ISF compartment

$$V_{IS}^{brain}\cdot\frac{dC_{IS}^{brain}}{dt}=\left(1-\sigma_V^{BBB}\right)\cdot Q_{ISF}^{brain}\cdot C_p^{brain}-\left(1-\sigma_L^{brainISF}\right)\cdot Q_{ISF}^{brain}\cdot C_{IS}^{brain}-Q_{ISF}^{brain}\cdot C_{IS}^{brain}+Q_{ISF}^{brain}\cdot C_{SAS}^{brain}+CL_{up}^{brain}\cdot f_{BBB}\cdot V_{ES}^{brain}\cdot(1-FR)\cdot C_{BBB_{bound}}^{brain}-CL_{up}^{brain}\cdot f_{BBB}\cdot V_{ES}^{brain}\cdot C_{IS}^{brain} \tag{7}$$

Blood cells compartment

$$V_{BC}^{brain}\cdot\frac{dC_{BC}^{brain}}{dt}=Q_{BC}^{brain}\cdot C_{BC}^{lung}-Q_{BC}^{brain}\cdot C_{BC}^{brain} \tag{8}$$

Cerebrospinal fluid (CSF)

Unbound mAb in endosomal compartment at brain–CSF barrier (BCSFB)

$$V_{BCSFB}^{brain}\cdot\frac{dC_{BCSFB_{unbound}}^{brain}}{dt}=CL_{up}^{brain}\cdot f_{BCSFB}\cdot V_{ES}^{brain}\cdot C_p^{brain}+f_{LV}\cdot CL_{up}^{brain}\cdot(1-f_{BBB})\cdot V_{ES}^{brain}\cdot C_{LV}^{brain}+(1-f_{LV})\cdot CL_{up}^{brain}\cdot(1-f_{BBB})\cdot V_{ES}^{brain}\cdot C_{TFV}^{brain}-V_{BCSFB}^{brain}\cdot k_{on}^{FcRn}\cdot C_{BCSFB_{unbound}}^{brain}\cdot FcRn_{free}^{BCSFB}+V_{BCSFB}^{brain}\cdot k_{off}^{FcRn}\cdot C_{BCSFB_{bound}}^{brain}-V_{BCSFB}^{brain}\cdot k_{deg}\cdot C_{BCSFB_{unbound}}^{brain} \tag{9}$$

Note: $f_{LV}=\frac{V_{LV}^{brain}}{V_{LV}^{brain}+V_{TFV}^{brain}}$

Bound mAb in endosomal compartment at brain–CSF barrier (BCSFB)

$$V_{BCSFB}^{brain}\cdot\frac{dC_{BCSFB_{bound}}^{brain}}{dt}=-CL_{up}^{brain}\cdot(1-f_{BBB})\cdot V_{ES}^{brain}\cdot C_{BCSFB_{bound}}^{brain}+V_{BCSFB}^{brain}\cdot k_{on}^{FcRn}\cdot C_{BCSFB_{unbound}}^{brain}\cdot FcRn_{free}^{BCSFB}-V_{BCSFB}^{brain}\cdot k_{off}^{FcRn}\cdot C_{BCSFB_{bound}}^{brain} \tag{10}$$

Lateral ventricle

$$V_{LV}^{brain}\cdot\frac{dC_{LV}^{brain}}{dt}=\left(1-\sigma_V^{BCSFB}\right)\cdot f_{LV}\cdot Q_{CSF}^{brain}\cdot C_p^{brain}+f_{LV}\cdot Q_{ISF}^{brain}\cdot C_{IS}^{brain}-\left(f_{LV}\cdot Q_{CSF}^{brain}+f_{LV}\cdot Q_{ISF}^{\text{brain}}\right)\cdot C_{LV}^{brain}-f_{LV}\cdot CL_{up}^{brain}\cdot(1-f_{BBB})\cdot V_{ES}^{brain}\cdot C_{LV}^{brain}+f_{LV}\cdot CL_{up}^{brain}\cdot(1-f_{BBB})\cdot V_{ES}^{brain}\cdot(1-FR)\cdot C_{BCSFB_{bound}}^{brain} \tag{11}$$

Third forth ventricle

$$V_{TFV}^{brain}\cdot\frac{dC_{TFV}^{brain}}{dt}=\left(1-\sigma_V^{BCSFB}\right)\cdot(1-f_{LV})\cdot Q_{CSF}^{brain}\cdot C_p^{brain}+(1-f_{LV})\cdot Q_{ISF}^{brain}\cdot C_{IS}^{brain}-\left(Q_{CSF}^{brain}+Q_{ISF}^{\text{brain}}\right)\cdot C_{TFV}^{brain}-(1-f_{LV})\cdot CL_{up}^{brain}\cdot(1-f_{BBB})\cdot V_{ES}^{brain}\cdot C_{TFV}^{brain}+(1-f_{LV})\cdot CL_{up}^{brain}\cdot(1-f_{BBB})\cdot V_{ES}^{brain}\cdot(1-FR)\cdot C_{BCSFB_{bound}}^{brain}+\left(f_{LV}\cdot Q_{CSF}^{brain}+f_{LV}\cdot Q_{ISF}^{\text{brain}}\right)\cdot C_{LV}^{brain} \tag{12}$$

Cisterna magna

$$V_{CM}^{brain}\cdot\frac{dC_{CM}^{brain}}{dt}=\left(Q_{CSF}^{brain}+Q_{ISF}^{\text{brain}}\right)\cdot\left(C_{TFV}^{brain}-C_{CM}^{brain}\right) \tag{13}$$

Subarachnoid space

$$V_{SAS}^{brain}\cdot\frac{dC_{SAS}^{brain}}{dt}=\left(Q_{CSF}^{brain}+Q_{ISF}^{\text{brain}}\right)\cdot C_{CM}^{brain}-\left(1-\sigma_L^{SAS}\right)\cdot Q_{CSF}^{brain}\cdot C_{SAS}^{brain}-Q_{ISF}^{brain}\cdot C_{SAS}^{brain} \tag{14}$$

A typical tissue "i"

Blood cells compartment

$$V_{BC}^{i}\cdot\frac{dC_{BC}^{i}}{dt}=Q_{BC}^{i}\cdot C_{BC}^{j}-Q_{BC}^{i}\cdot C_{BC}^{i} \tag{15}$$

Plasma compartment

$$V_p^i\cdot\frac{dC_p^i}{dt}=Q_p^i\cdot C_p^j-\left(Q_p^i-L^i\right)\cdot C_p^i-\left(1-\sigma_V^i\right)\cdot L^i\cdot C_p^i-CL_{up}^i\cdot C_p^i+CL_{up}^i\cdot FR\cdot C_{E_{bound}}^i \tag{16}$$

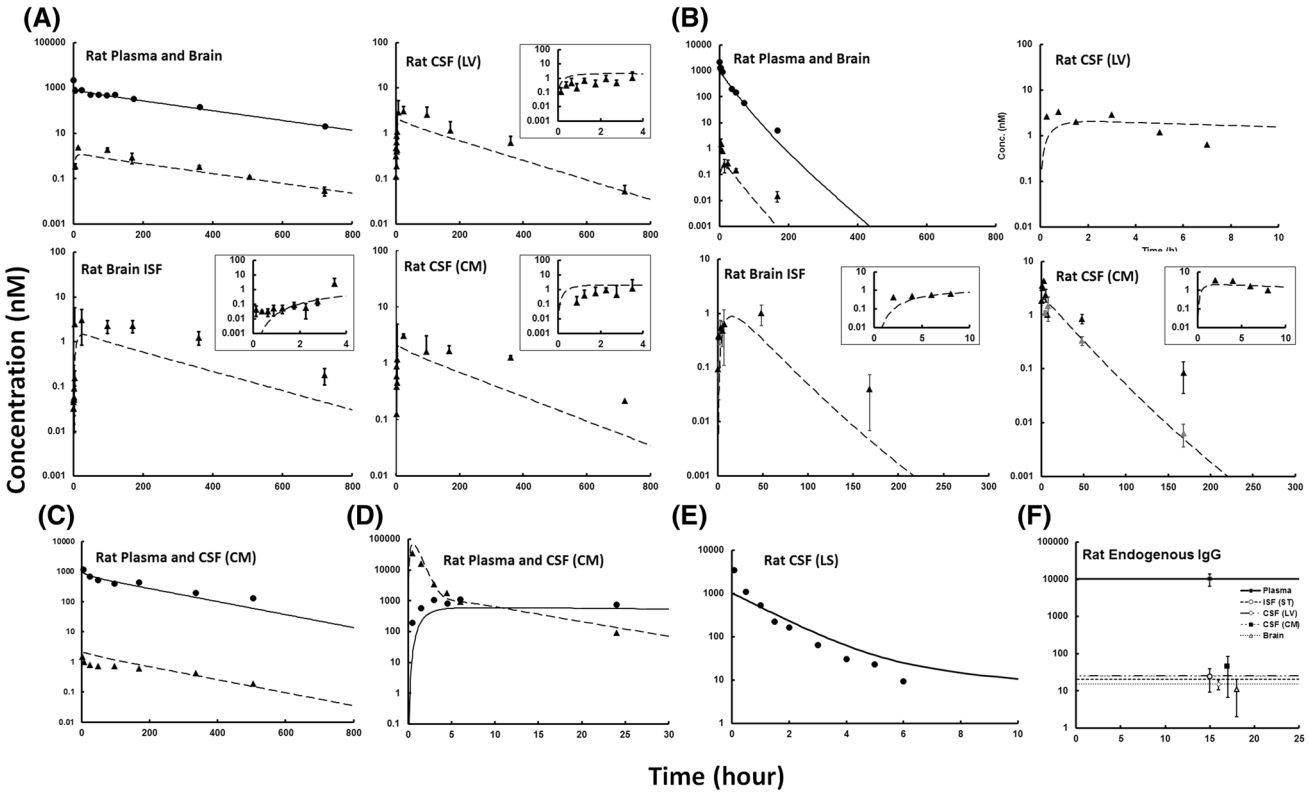

Fig. 2 PK of nonspecific mAbs in rats. The figure shows observed (solid dots) and model fitted (solid lines) PK profiles of mAbs in rats. **a** PK of nonspecific mAb in plasma, brain ISF, CSF (lateral ventricle and cisterna magna), and whole brain, after *i.v.* administration of 10 mg/kg dose. **b** PK of FcRn nonbinding mAb in plasma, brain ISF, CSF (LV and CM), and whole brain, after *i.v.* administration of 10 mg/kg dose **c** PK of nonspecific mAb in plasma and CSF_{CM} after *i.v.* administration of 10 mg/kg dose. **d** PK of nonspecific mAb in CSF_{CM} after intracerebroventricular administration of 0.5 mg/kg dose. **e** PK of anti-ganglioside GD2 mAb in CSF_{LS} after intrathecal administration of 1 mg/kg dose, and **f** Rat endogenous IgG concentration in plasma and different regions of the brain (error bars represent standard deviation)

Table 3 Final parameter estimates

Parameter	Final estimate (CV%)	Units	Description
k_{deg}	26.6 (12.7)	1/h	Degradation rate constant of unbound mAb in the endosomal space
CL_{up}^{brain}	0.03 (38.2)	L/h/L	Pinocytosis rate constant of mAb molecules per unit endosomal volume of brain capillaries
σ_V^{BCSFB}	0.9974 (0.039)	–	Reflection coefficient for blood–CSF barrier

CV Coefficient of variation, *BCSFB* blood–CSF barrier, *CSF* cerebrospinal fluid

Note: $CL_{up}^{i} = CL_{up} \cdot V_{ES}^{i}$

Unbound mAb in endosomal compartment

$$V_{ES}^{i} \cdot \frac{dC_{E\_unbound}^{i}}{dt} = CL_{up}^{i} \cdot C_{p}^{i} + CL_{up}^{i} \cdot C_{IS}^{i} - V_{ES}^{i} \cdot k_{on} \cdot C_{E\_unbound}^{i} \cdot FcRn_{free}^{i} + V_{ES}^{i} \cdot k_{off} \cdot C_{E\_bound}^{i} - k_{deg} \cdot C_{E\_unbound}^{i} \cdot V_{ES}^{i} \quad (17)$$

Bound mAb in endosomal compartment

$$V_{ES}^{i} \cdot \frac{dC_{E\_bound}^{i}}{dt} = V_{ES}^{i} \cdot k_{on} \cdot C_{E\_unbound}^{i} \cdot FcRn_{free}^{i} - V_{ES}^{i} \cdot k_{off} \cdot C_{E\_bound}^{i} - CL_{up}^{i} \cdot C_{E\_bound}^{i} \quad (18)$$

Table 4 Median percentage prediction error

Species	Dataset	$AUC_{0\text{-tlast}}$	%PE vlue
Rat	Fig. 2a	Brain homogenate	−48
		CSF_{CM}	−47.4
		CSF_{LV}	−42.5
		ISF_{ST}	−65.6
		Plasma	−12.3
	Fig. 2b	Brain homogenate	−67.4
		CSF_{CM}	−46.3
		CSF_{LV}	48.9
		ISF_{ST}	−61.6
		Plasma	−28.1
	Fig. 2c	Plasma	−13.2
		CSF_{CM}	36.1
	Fig. 2d	Plasma	−40.6
		CSF_{CM}	81.3
	Fig. 2e	$CSF_{SAS/LS}$	−23.7
Mice	Fig. 3a	Plasma	30.6
		Brain homogenate	65.4
	Fig. 3b	Plasma	65.8
		Brain homogenate	92.1
Monkey	Fig. 4a (1st dose)	Plasma	8.5
		CSF_{CM}	−60
	Fig. 4a (4th dose)	Plasma	−26.2
		CSF_{CM}	−58.2
	Fig. 4b	Css of plasma	−2.4
		Css of CSF_{CM}	−5.5
	Fig. 4c	Plasma	−30.7
		CSF_{CM}	43.2
Human	Fig. 5a	Plasma	14.1
		$CSF_{SAS/LS}$	47.5
	Fig. 5b	Plasma	18
		$CSF_{SAS/LS}$	117.7
	Fig. 5c	Plasma	0.2
		$CSF_{SAS/LS}$	88.1

AUC Area under a curve, *Css* concentration at the steady state, CSF_{CM} cerebrospinal fluid at the cisterna magna, CSF_{LV} cerebrospinal fluid at the lateral ventricle, ISF_{ST} brain interstitial fluid at the striatum, $CSF_{SAS/LS}$ cerebrospinal fluid at the subarachnoid space/lumbar spine, *%PE* percentage of prediction error

Interstitial Compartment

$$V_{IS}^{i}\cdot\frac{dC_{IS}^{i}}{dt}=(1-\sigma_{V}^{i})\cdot L^{i}\cdot C_{p}^{i}-(1-\sigma_{L}^{i})\cdot L^{i}\cdot C_{IS}^{i}+CL_{up}^{i}\cdot(1-\mathrm{FR})\cdot C_{E\_bound}^{i}-CL_{up}^{i}\cdot C_{IS}^{i} \quad (19)$$

FcRn equation

$$V_{ES}^{i}\cdot\frac{dFcRn_{free}^{i}}{dt}=k_{0ff}\cdot C_{E\_bound}^{i}\cdot V_{ES}^{i}-k_{on}\cdot C_{E\_unbound}^{i}\cdot FcRn_{free}^{i}\cdot V_{ES}^{i}+CL_{up}^{i}\cdot C_{E\_bound}^{i} \quad (20)$$

Above, Eqs. 15–19 describe a typical tissue compartment, and the subscript "*i*" refers to the individual tissue being considered for the analysis. For all the tissues except lung and liver the subscript "*j*" in Eqs. 15 and 16 refers to the lung concentration, whereas for the lung subscript "*j*" refers to plasma/blood cell concentrations. Due to the unique anatomical arrangement of the liver the vascular space in this tissue compartment is described differently using the following equations.

Liver compartment

Vascular space plasma

$$\begin{aligned}V_{p}^{liver}\cdot\frac{dC_{p}^{liver}}{dt}&=Q_{p}^{liver}\cdot C_{p}^{lung}+\left(Q_{p}^{spleen}-L^{spleen}\right)\cdot C_{p}^{spleen}+\left(Q_{p}^{pancreas}-L^{pancreas}\right)\cdot C_{p}^{pancreas}+\left(Q_{p}^{SI}-L^{SI}\right)\cdot C_{p}^{SI}\\&+\left(Q_{p}^{LI}-L^{LI}\right)\cdot C_{p}^{LI}-\left(\left(\mathrm{Q_{p}}^{liver}-L^{liver}\right)+\left(Q_{p}^{spleen}-L^{spleen}\right)+\left(Q_{p}^{pancreas}-L^{pancreas}\right)\right.\\&\left.+\left(Q_{p}^{SI}-L^{SI}\right)+\left(Q_{p}^{LI}-L^{LI}\right)\right)\cdot C_{p}^{liver}-\left(1-\sigma_{V}^{liver}\right)\cdot L^{liver}\cdot C_{p}^{liver}-CL_{up}^{liver}\cdot C_{p}^{liver}+CL_{up}^{liver}\cdot FR\cdot C_{E_{bound}}^{liver}\end{aligned} \quad (21)$$

Vascular space blood cells

$$\begin{aligned}V_{BC}^{liver}\cdot\frac{dC_{BC}^{liver}}{dt}&=Q_{BC}^{liver}\cdot C_{BC}^{lung}+Q_{BC}^{spleen}\cdot C_{BC}^{spleen}+Q_{BC}^{pancreas}\cdot C_{BC}^{pancreas}+Q_{BC}^{SI}\cdot C_{BC}^{SI}+Q_{BC}^{LI}\cdot C_{BC}^{LI}\\&-\left(Q_{BC}^{liver}+Q_{BC}^{spleen}+Q_{BC}^{pancreas}+Q_{BC}^{SI}+Q_{BC}^{LI}\right)\cdot C_{BC}^{liver}\end{aligned} \quad (22)$$

Model parameters Values of brain specific model parameters along with references associated with those parameters are listed in Table 2. Values of all other model parameters are listed in Supplementary Tables 2, 3, 4, 5, and 6. Whenever multiple different values were reported for brain related physiological parameters (e.g. ISF production rate and cerebral blood flow), the median value was used for the PBPK model (shown as underlined values in Table 2). Lymph flow for each tissue was fixed to 0.2% of plasma flow. The vascular reflection coefficient (σ_{V}^{i}) was

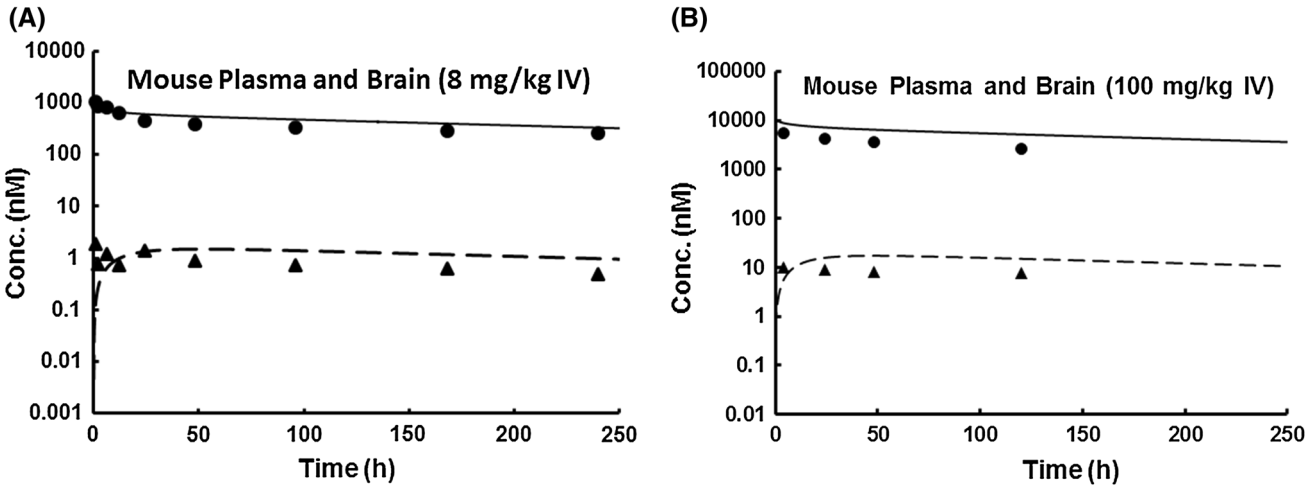

Fig. 3 PK of nonspecific mAbs in mice. The figure shows observed (solid dots) and model predicted (solid lines) PK profiles of mAbs in mice. **a** PK of nonspecific mAb in plasma and brain after *i.v.* administration of 8 mg/kg dose, and **b** PK of nonspecific mAb in plasma and brain after *i.v.* administration of 100 mg/kg dose

set to 0.95 for lung, heart, muscle, skin, adipose, large intestine and others compartment; 0.9 for kidney, thymus, small intestine and pancreas; and 0.85 for spleen, liver and bone [56]. The lymphatic reflection coefficient (σ_L^i) was set to 0.2 for all tissues [25]. The fraction of FcRn bound antibody that recycles to vascular space (*FR*) was set to 0.715 [53]. Association rate constant between IgG and FcRn (k_{on}) were $8.06 \cdot 10^7$, $8.00 \cdot 10^8$, $7.92 \cdot 10^8$ and $5.59 \cdot 10^8 M^{-1}h^{-1}$ for mouse, rat, monkey and human; and dissociation rate constant (k_{off}) were 6.55, 144, 46.8 and 23.9 h^{-1}, respectively. The concentration of FcRn in the endosomal space ($FcRn_{free}^i$) and the proportionality constant (C_LNLF) between the lymph node flow (L^{LN}) and the plasma flow (Q_p^{lung}) were $4.982 \cdot 10^{-5}$ M and 9.1, respectively [27]. The rate of pinocytosis per unit endosomal space (CL_{up}) was set to 0.55 L/h/L for all the tissue, except for brain.

Parameter estimation and model evaluation Plasma, brain, CSF, and ISF PK of mAbs in rat obtained from different published and in-house studies were simultaneously fitted with the brain PBPK model to estimate 3 unknown parameters. Two parameters associated with antibody disposition in the brain and one parameter associated with systemic disposition of mAb were estimated. These parameters include: (a) the pinocytosis rate of mAb per unit endosomal volume of brain vascular endothelium and choroid plexus epithelium cells (i.e. CL_{up}^{brain}) (b) the degree of impermeability of BCSFB (i.e. σ_V^{BCSFB}), and (c) antibody degradation rate in endosome (i.e. k_{deg}). The model was fitted to the data using the maximum likelihood estimation method in ADAPT-5 software (BMSR, CA), as previously described [27]. The following variance model was used:

$$\mathrm{Var(t)} = \left(\sigma_{\mathrm{Intercept}} + \sigma_{Slope} \cdot Y(t)\right)^2$$

where the variance Var(t) is associated with the model output Y(t) using two variance parameters, $\sigma_{\mathrm{Intercept}}$ and σ_{Slope}. The final model structure and parameter estimates were determined using standard model fitting criteria: visual inspection, observed versus predicted plot, predicted versus residual plot, and coefficient of variation (CV%) of the estimated parameters.

In order to evaluate the quality of translated mouse, monkey, and human brain PBPK models, the model predicted PK profiles were superimposed over the observed data. In addition, for a quantitative comparison of observed and model predicted data, median percentage prediction error (%PE) was computed for each profile using the following equation: $\%\mathrm{PE} = \frac{|AUC_{pred} - AUC_{obs}|}{AUC_{obs}} \cdot 100\%$. In this equation, AUC_{Pred} is the AUC of model predicted PK profile and AUC_{Obs} is the AUC of observed PK profile.

Global sensitivity analysis (GSA) In order to understand the importance of certain model parameters toward brain disposition of mAbs, a global sensitivity analysis was performed as described before [57]. Five parameters were chosen for GSA, which included three estimated model parameters (k_{deg}, CL_{up}^{brain},σ_V^{BCSFB}) and two physiological parameters (Q_{CSF}, Q_{ISF}) that might alter under pathological conditions. In order to ensure the value of σ_V^{BCSFB} do not exceed 1 during the analysis, the value of '$1 - \sigma_V^{BCSFB}$' was altered during GSA. The total sensitivity index was estimated by the SOBOL method [58] using IQM toolbox in Matlab. The model was simulated by perturbating

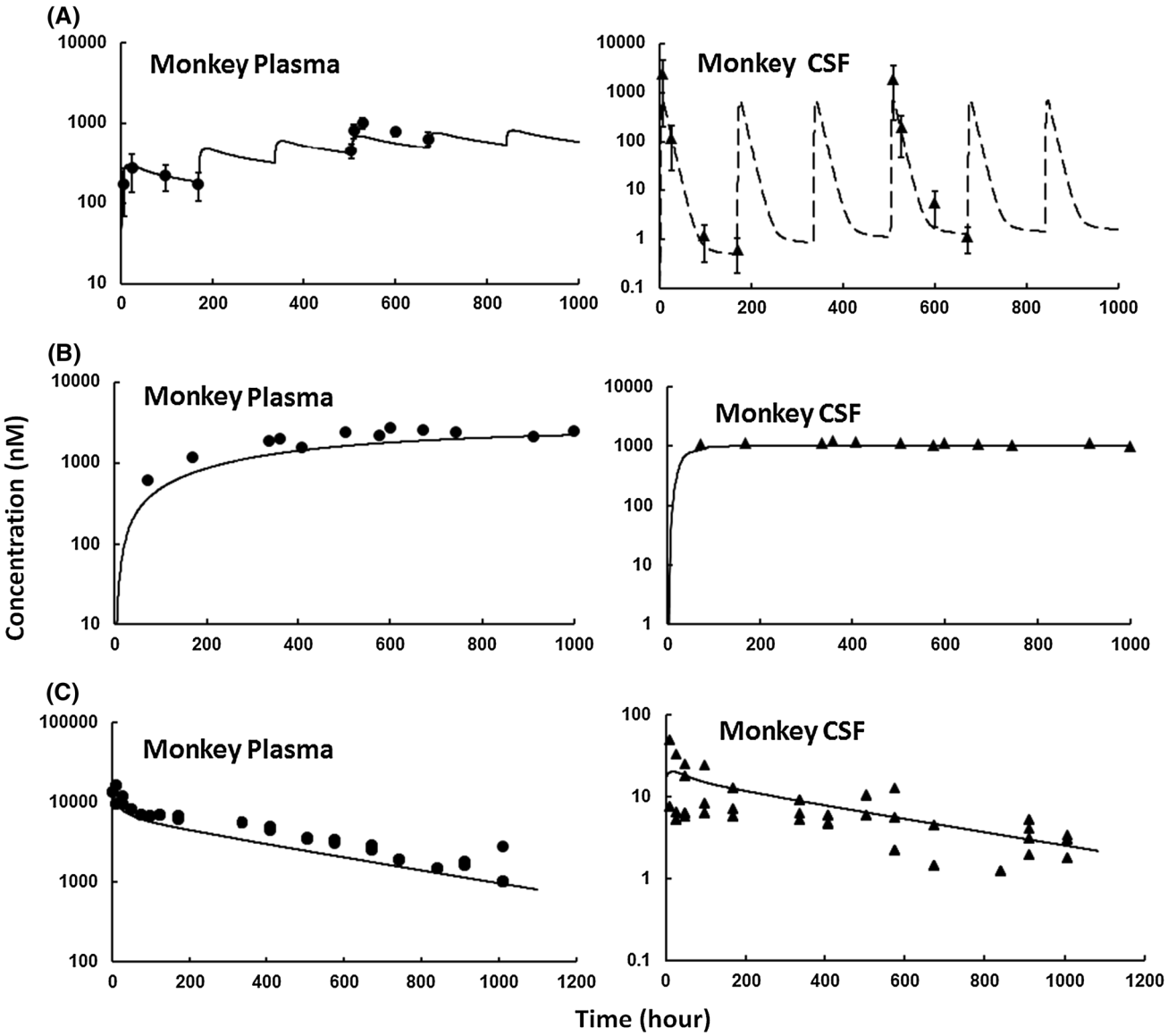

Fig. 4 PK of nonspecific mAbs in monkeys. Figure shows observed (solid dots) and model predicted (solid lines) PK profiles of mAbs in monkeys. **a** PK of nonspecific mAb in plasma and CSF_{CM} after intrathecal injection of 15 mg dose once per week (0.24 mg/g brain weekly). **b** PK of nonspecific mAb in plasma and CSF_{CM} after intracerebroventricular infusion at a rate of 1.68 mg/kg/h over 6 weeks, and **c** the PK of anti-aggregated α-synuclein mAb in plasma and CSF after *i.v.* administration of 100 mg/kg dose

parameter values generated by Latin hypercube sampling, using a sample size of 100,000. An integrated algorithm of SOBOL method was applied to evaluate the total effect of parameters on the output, by considering the higher order interaction effects. MAb PK in plasma, ISF, CSF_{CM}, and whole brain were chosen as model outputs for GSA.

Results

Development of rat PBPK model

As shown in Fig. 2 the brain PBPK model was able to simultaneously characterize all plasma, brain, ISF, and CSF PK profiles of mAbs in rats reasonably well. Estimated parameter values are provided in Table 3, and %PE values for all datasets are provided in Table 4. Three model parameters were also estimated with good confidence. The parameter characterizing the degradation of unbound mAb in the endosomal space (k_{deg}) was estimated to be 26.6 h^{-1} with %CV of 12.7. The parameter characterizing

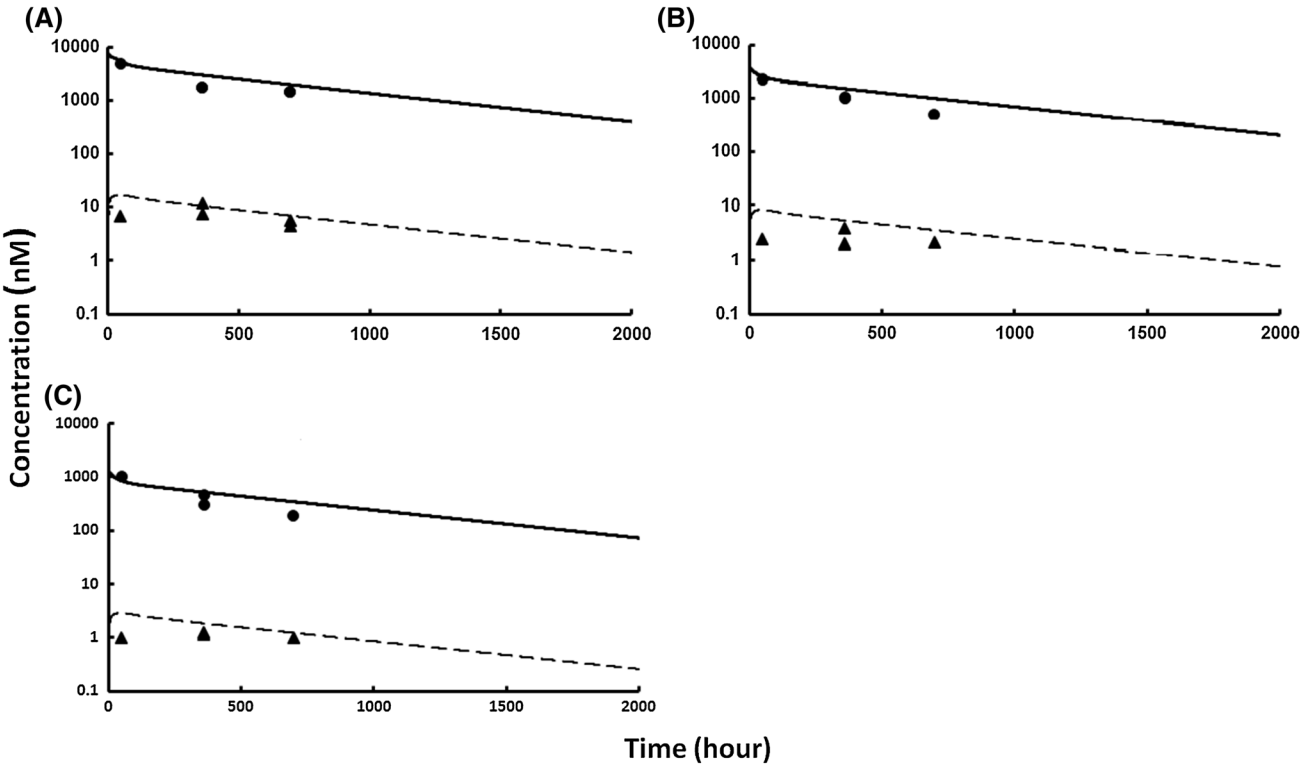

Fig. 5 PK of nonspecific mAb in human. Figure shows observed (solid dots) and model predicted (solid lines) plasma and CSF PK profiles of a mAb in human after intravenous infusion of **a** 36 **b** 18, and **c** 6 mg/kg doses

pinocytosis rate of mAb molecules per unit endosomal volume of brain capillaries (CL_{up}^{brain}) was estimated to be 0.03 L/h/L with %CV of 38.2. The reflection coefficient for BCSFB (σ_V^{BCSFB}) was estimated to be 0.9974 with %CV of 0.039.

Figure 2a shows observed and model predicted plasma, whole brain, ISF_{ST}, CSF_{LV}, and CSF_{CM} PK profiles obtained after *i.v.* administration of 10 mg/kg trastuzumab in wild-type rats. The %PE values for plasma, brain homogenate, ISF_{ST}, CSF_{LV}, and CSF_{CM} were found to be 12.35, 48.0, 65.7, 42.5, and 47.4, respectively. Figure 2b shows the observed and model predicted PK profiles for FcRn nonbinding trastuzumab after 10 mg/kg *i.v.* dose. As evident from Fig. 2, removal of FcRn mediated recycling process resulted in enhanced clearance of trastuzumab. The model was able to characterize plasma and brain PK of FcRn nonbinding trastuzumab reasonably well. The %PE values for plasma, brain homogenate, ISF_{ST}, CSF_{LV}, and CSF_{CM} were found to be 28.1, 67.4, 61.6, 48.9, and 46.3, respectively. Figure 2c shows observed and model predicted plasma and CSF_{CM} PK profiles for another non-specific antibody (399 H0/L0) in rats after 10 mg/kg *i.v.* dose. Both CSF_{CM} (%PE = 36.14) and plasma (%PE = 13.20) PK profiles were characterized well. Two additional datasets with different routes of administration were also included for better optimization of the model. Figure 2d Shows observed and model predicted plasma and CSF_{CM} PK profiles for a non-specific mAb in rat after ICV administration of 10 mg/kg dose. The %PE values for plasma and CSF_{CM} were found to be 40.6 and 81.3, respectively. Figure 2e shows observed and model predicted CSF_{LS} PK profile for another non-specific mAb in rat after intrathecal administration of 0.1 mg/kg dose. The model was able to characterize this profile as well, with a %PE value of 23.7. The brain PBPK model was also simultaneously fitted to endogenous IgG concentrations in different regions of rat brain (Fig. 2f). Plasma endogenous IgG concentrations were fixed to the reported value of 1534 µg/mL [13], and ISF, CSF_{LV}, CSF_{CM}, and brain homogenate concentrations were used to estimate the model parameters. While the model underpredicted CSF_{CM} concentrations (CSF_{CM_pred} 3.8 µg/mL and CSF_{CM_obs} 6.8–14.7 µg/mL), ISF (ISF_{pred} 3.1 µg/mL and ISF_{obs} 3.7 µg/mL), CSF_{LV} (CSF_{LV_pred} 3.8 µg/mL and CSF_{LV_obs} 3.7 µg/mL), and brain homogenate ($Brain_{pred}$ 2.3 µg/mL and $Brain_{obs}$ 1.7 µg/mL) concentrations were reasonably well predicted.

Validation of mouse PBPK model

Figure 3 shows observed and model predicted plasma and brain PK profiles of non-specific mAbs in mice after 8

(Fig. 3a) or 100 (Fig. 3b) mg/kg *i.v.* dose. The model was able to predict plasma and brain PK profiles of both mAbs reasonably well. At very early time points though, there was a trend towards underprediction of brain concentrations. Nonetheless, %PE values for brain PK of mAbs at 8 and 100 mg/kg dose were found to be 65.4 and 92.1, respectively.

Validation of monkey PBPK model

Figure 4a shows observed and model predicted plasma and CSF PK profiles for a non-specific mAb in monkey after multiple intrathecal administration of 15 mg dose per week. Both plasma and CSF PK profiles were well predicted with %PE values of 8.5 and 60.0, respectively. Figure 4b shows observed and model predicted plasma and CSF PK profiles for another non-specific mAb in monkey after ICV infusion. The model was able to accurately predict these PK profiles as well, with %PE values of 2.4 and 5.5 for steady state plasma and CSF concentrations, respectively. Figure 4c shows observed and model predicted plasma and CSF_{CM} PK profiles for BIIB054 in monkey after *i.v.* administration of 100 mg/kg dose. This antibody specifically binds to aggregated α-synuclein, which is less likely to be present in healthy monkeys. Both plasma and CSF PK profiles of BIIB054 were predicted accurately by the model, with %PE values of 30.7 and 43.2, respectively

Validation of human PBPK model

Figure 5 shows observed and model predicted plasma and CSF_{LS} PK profiles of a non-specific mAb in human after *i.v.* administration of 36, 18, and 6 mg/kg dose. All the PK profiles were reasonably well predicted by the PBPK model, however, there was a trend towards slight over prediction of CSF_{LS} concentrations at the very early time points. Plasma PK profiles for all doses were predicted with %PE values less than 20, and CSF_{LS} PK profiles were predicted with %PE values ranging from 47.5 (for 36 mg/kg dose) to 117.7 (for 18 mg/kg dose). The model predicted plasma/CSF ratio for endogenous human antibody of ~ 300 was also similar to the reported value of 350–1000 for human IgG4 and IgG1 [43]. This plasma/CSF ratio is also similar to the clinically reported value of 292–332 for anti-HER2 mAb trastuzumab in human [6]. In general, %PE values from all the datasets (Table 4) suggest that the platform PBPK model is able to predict brain and CSF exposure of mAbs in all the species within threefold of the observed values.

Global sensitivity analysis

Figure 6 shows the results of the GSA performed on mouse, rat, monkey, and human PBPK models. In general, the outcome of the analysis did not change based on the animal species. As expected, among all five parameters, k_{deg} was found to be the most important for determining plasma exposure of mAbs. The exposure of mAb in brain ISF was found to be most sensitive to mAb uptake clearance (CL_{up}^{brain}) by pinocytosis in brain capillaries. MAb exposure in brain ISF was also sensitive to Q_{ISF}. The exposure of mAb in brain CSF (i.e. CSF_{CM}) was found to be most sensitive to BCSFB reflection coefficient σ_V^{BCSFB}.

Discussion

In this manuscript, we have presented the first ever PBPK model for mAb disposition in the brain by augmenting our previously published platform PBPK model for mAbs [27]. As such, the proposed model is capable of simultaneously characterizing plasma, brain, and whole-body PK of mAbs in multiple animal species and human. The model is built using published and in-house PK data obtained from brain disposition studies of mAbs in rats. This includes unprecedented PK data on the disposition of mAb in different regions of the brain obtained using our recently developed state-of-the-art large-pore microdialysis technique [13]. The rat PBPK model is translated to mouse, monkey, and human, and the translated models are validated using published brain disposition data for various mAbs and endogenous IgG.

The brain PBPK model (Fig. 1) assumes that once the mAb enters brain vascular space it needs to cross one of the two major barriers to enter into the brain, the BBB, which is lining the cerebral microvessels and dispersed throughout the brain parenchyma, or BCSFB in the choroid plexuses that is located within the ventricles. BBB is formed cooperatively by the layer of endothelial cells, pericytes, and astrocyte (glial) endfeet [51]. Endothelial cells are connected to each other via very tight junctions that effectively block paracellular transport of molecules and ions. In fact, it has been reported that BBB vasculature has one of the lowest paracellular diffusion and pinocytosis rate in the whole body [59]. Accordingly, we have assumed that σ_V^{BBB} is 1, and the estimated value of brain-specific pinocytosis rate (CL_{up}^{brain} = 0.03047 L/h/L) was found to be ~ 18 times lower than the pinocytosis rate for capillaries in other tissues (CL_{up} = 0.55 L/h/L). The model also incorporates FcRn mediated transcytosis and efflux of mAb via BBB endosomal space. Since the FR value for FcRn bound mAb in all tissues, including brain, is 0.715, the

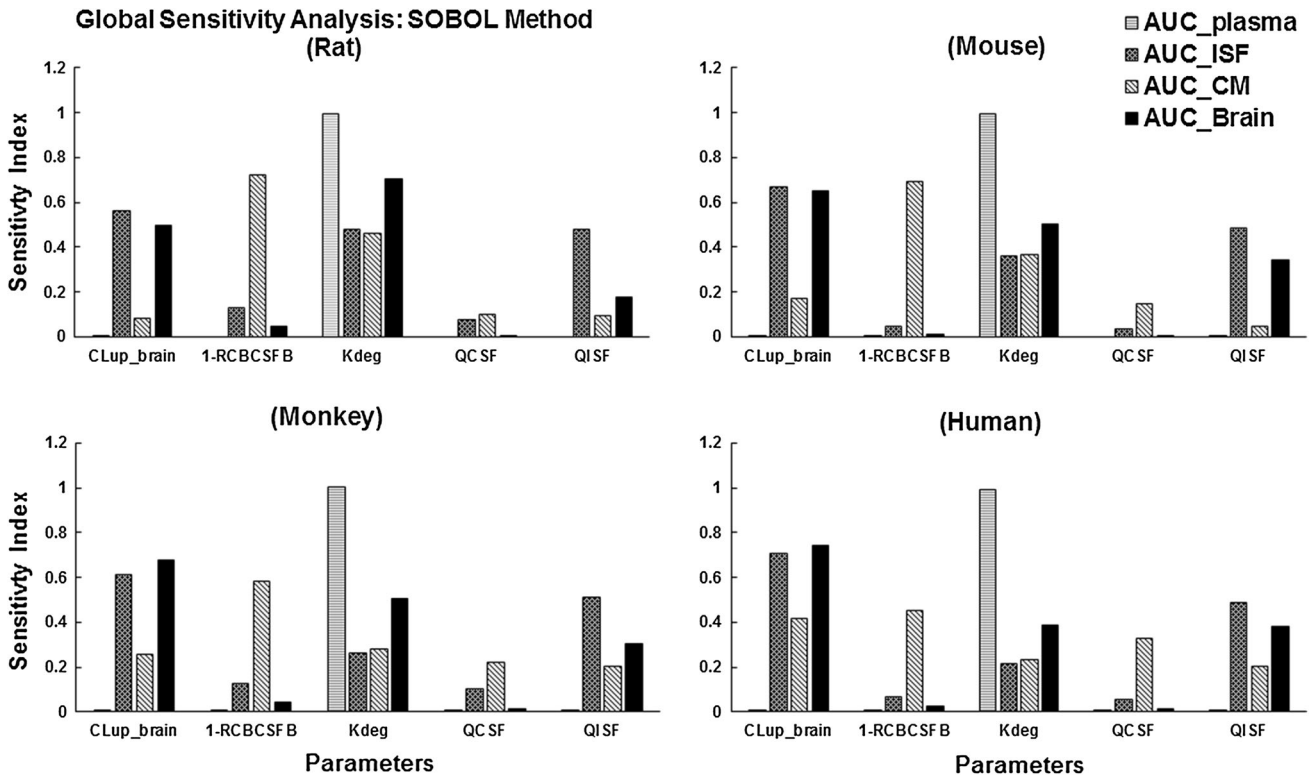

Fig. 6 Global sensitivity analysis of mouse, rat, monkey, and human PBPK models. Five parameters were selected to perform global sensitivity. CL_{up_brain}: pinocytosis rate at blood–brain barrier and blood–CSF barrier, $1\text{-}RC_{BCSFB}$: the reflection coefficient at blood–CSF barrier, K_{deg}: degradation rate of free mAb in endosome, Q_{CSF}: cerebrospinal fluid flow rate, Q_{ISF}: brain interstitial fluid flow rate. The sensitivity index was calculated by the change of the area under the curve (AUC) in plasma, brain ISF, CSF_{CM}, and whole brains

model inherently assumes that higher fraction of FcRn bound mAb shuttles back to the vascular space [27, 60]. As such, the model may be able to capture FcRn-mediated efflux of mAb from the brain that is observed in some unidirectional experiments following intracranial injections [35–37]. On the other hand, FcRn may be able to facilitate influx of mAbs across BBB as well, which remains to be evaluated [61].

The PBPK model also incorporates FcRn mediated processes at the BCSFB, since it is known that FcRn is expressed in choroid plexus epithelium cells [35]. These cuboidal epithelial cells of BCSFB forms the real barrier between blood and CSF at the ventricles to restrict paracellular transport of macromolecules, since the endothelium cells of brain microvessels in this region (also known as stroma) are fenestrated. Consistent with the literature on CSF secretion, circulation, and reabsorption [30, 32, 51, 62], the model assumes that CSF is produced at the apical membrane of choroid plexuses [63, 64]. Since BCSFB is known to be leakier than BBB, it is assumed that it may contribute to direct entry of mAb into the CNS via CSF flow. This hypothesis is supported by our recently published PK data, where we observed a faster entry of mAb into the LV compared to brain ISF following systemic administration of mAb [13]. As such, σ_V^{BCSFB} was not fixed to 1, and it was estimated to be 0.9974 by fitting the model to the data. The model also accounts for clearance of mAb from CSF via drainage to multiple peripheral lymph nodes or vessels including meningeal lymphatic vasculature [65, 66]. In addition, brain glymphatic system [30–32, 66] was also accounted for in the model, which allowed bulk flow of mAb from SAS to brain interstitial space along the perivascular region. Since measurements of flow rates and volumes of the proposed perivascular spaces and CNS lymphatic vessels are not available, the model was simplified by including bulk flow of CSF into brain ISF and a collective lymphatic clearance of mAb from CNS. The model also accounted for production of CSF from ISF, and assumed that 10% of CSF is produced from brain ISF [51]. This was incorporated as the flow of fluid from brain ISF to LV and TFV via ependymal cellular layer.

As shown in Fig. 2 and Table 3, the PBPK model was able to simultaneously characterize all the published and in-house mAb PK data in rats reasonably well, while estimating only 3 model parameters. Considering that the model consists of numerous parameters that are fixed a priori, and the data used to fit the model is mean data that

comes from diverse sources, the performance of the model in such a low degree of freedom is testament to predictive capabilities of systems PK models. Careful comparison of observed and model predicted PK profiles reveal that while there was obvious over or under prediction of certain PK profiles, there was no consistent trend towards model deviation, and all the predicted exposures were within threefold of the observed data. In addition, the model was able to accurately capture PK profiles obtained following systemic or local administration of mAbs in the brain, which provided more confidence in the model's ability to capture important process responsible for the disposition of mAbs throughout the brain. As shown in Figs. 3, 4, 5 and Table 3, when the brain PBPK model was translated to mouse, monkey, and human, it was able to a priori predict the PK of various mAbs in all three species reasonably well. Of note, since there is no data reported on the PK of mAbs in ISF compartment of all these species, the validation of the model mainly hinges on CSF and brain homogenate PK. Nonetheless, there was no consistent deviation towards over or under prediction of PK for any brain compartment, and the model was able to predict all the PK datasets within threefold. While the final model presented here provides an unprecedented quantitative tool for characterization and prediction of mAb PK in the brain, in order to make the model even more robust and predictive there is need to generate more PK data using diverse set of mAbs across different animal species.

The proposed model can also be made more robust by experimentally validating or measuring unknown model parameters. As shown in Fig. 6, all three estimated parameters CL_{up}^{brain}, σ_V^{BCSFB}, and k_{deg}, can significantly affect ISF, CSF, and plasma PK of mAb, respectively. Thus, any method that can help us validate or experimentally measure these parameters can instill further confidence in the proposed PBPK model. It is important to note that while we have kept many model parameters (including the three estimated parameters) constant between animal species, these parameters can certainly change with species. As more and more information about these differences becomes available, the performance of the model for each animal species can be improved going forward. It is equally important to note that while the parameter values employed by us do not have variability incorporated around them, one can certainly use a population PBPK approach to obtain error envelop around the central tendencies simulated in this manuscript. However, getting an estimate on the extent and nature of variability around each parameter is very challenging.

Going forward the platform PBPK model for brain disposition of mAbs presented here could be augmented to account for target-mediated drug disposition (TMDD) [67] and receptor-mediated transcytosis (RMT) processes. For instance, the mAb PBPK model can be combined with a target disposition PBPK model [27, 29, 57] to characterize and predict how mAb and target interaction will affect the PK of each other. The model can also be used to account for enhanced brain efflux or intracellular degradation of mAb-target complex, similar to what is proposed for mAb-Aβ/tau protein complex [68–70]. MAbs that exploit RMT pathway to enhance brain delivery of mAbs (e.g. anti-TfR antibody) have gained tremendous attention lately [2]. These molecules have been evaluated in mice [17], rats [71], non-human primates [72, 73], and clinic [74]. Interestingly, the optimal affinity of anti-TfR mAbs required to maximize brain exposure differs in mice ($K_D \sim 32$ nM), rats ($K_D \sim 76$–108 nM), and monkeys ($K_D \sim 37$ nM). It is possible that this phenomenon may stem from different receptor turnover rates, internalization rates, and expression levels of TfR in different species, and incorporation of these processes in the platform PBPK model could able to explain the observed discrepancy between different species. Lastly, it is possible that many important model parameters (e.g. σ_V^{BBB}, σ_V^{BCSFB}, and Q_{ISF}) can alter in the pathophysiological state. This can significantly affect brain disposition of mAbs. If and when the direction and extent of changes in these parameters become available, one can easily incorporate them in the platform PBPK model to simulate the changes in brain exposure of mAbs associated with a disease state.

In summary, here we have presented a novel platform PBPK model to characterize brain disposition of mAbs by augmenting our previously published platform PBPK model for mAbs [27]. The model was built to account for state-of-the-art knowledge on the anatomy and physiology of brain, and majority of model parameters were fixed a priori based on the literature reported values. Unknown model parameters were estimated by fitting the model to published and in-house mAb PK data in rat brain. The rat PBPK model was translated to mouse, monkey, and human, and the translated models were able to a priori predict brain PK of mAbs within threefold of the observed data. The PBPK model presented here provides an unprecedent quantitative platform for preclinical-to-clinical translation of mAbs being developed for the treatment of CNS disorders. This platform model can be further expanded to account for target engagement, disease pathophysiology, and novel mechanisms, to support the discovery and development of novel CNS targeting mAbs.

Acknowledgements This work was supported by the Centre for Protein Therapeutics at University at Buffalo. D.K.S is supported by National Institute of Health Grant [GM114179] and [AI138195].

Appendix

A glossary of parameters used to build the platform brain PBPK model for mAbs

Parameter	Units	Definition
Q_p^i	L/h	Plasma flow to the tissue "i"
Q_{BC}^i	L/h	Blood cell flow to the tissue "i"
L^i	L/h	Lymph flow from the tissue "i"
Q_{CSF}^{brain},Q_{ISF}^{brain}	L/h	CSF and brain interstitial fluid formation rate
V^p, V^{BC}, V^{LN}	L	Volume of central plasma, central blood cell and lymph node compartments
V_{BBB}^{brain}, V_{BCSFB}^{brain}, V_{LV}^{brain}, V_{TFV}^{brain}, V_{CM}^{brain}, $V_{SAS(LS)}^{brain}$	L	Volume of BBB endosomal, BCSFB endosomal, LV, TFV, CM and SAS compartments
V_p^i, V_{BC}^i, V_{ES}^i, V_{IS}^i	L	Volume of vascular, blood cell, endosomal, and interstitial compartments for tissue "i"
C^p, C^{BC}, C^{LN}	M	Concentration of mAb in central plasma, central blood cell and lymph node compartments
$C_{BBB_{unbound}}^{brain}$, $C_{BBB_{bound}}^{brain}$, $C_{BCSFB_{unbound}}^{brain}$, $C_{BCSFB_{bound}}^{brain}$, C_{LV}^{brain}, C_{TFV}^{brain}, C_{CM}^{brain}, $C_{SAS(LS)}^{brain}$	M	Concentration of mAb in BBB endosomal (Unbound and Bound), BCSFB endosomal (Unbound and Bound), LV, TFV, CM and SAS compartments
C_p^i, C_{BC}^i, $C_{E\_unbound}^i$, $C_{E\_bound}^i$, C_{IS}^i	M	Concentration of mAb in vascular, blood cell, endosomal (Unbound and Bound), interstitial and cellular (Bound) compartments for tissue "i"
$FcRn_{free}^i$	M	Concentration of free FcRn in endosomal space
σ_V^i, σ_L^i	–	Vascular and lymph reflection coefficient
σ_V^{BBB}, σ_V^{BCSFB}	–	BBB and BCSFB vascular reflection coefficient
k_{on}	1/M/h	Association rate constant between mAb-FcRn
k_{off}	1/h	Dissociation rate constant between mAb-FcRn
FR	–	Fraction of FcRn bound mAb that recycles to the vascular space
f_{BBB},f_{BCSFB}	–	Surface area fractions of BBB and BCSFB
f_{LV}, f_{TFV}	–	Volume fractions of LV and TFV
SA_{BBB}, SA_{BCSFB}	L	Surface area of BBB and BCSFB
CL_{up}, CL_{up}^{brain}	L/h/L	Rate of pinocytosis and exocytosis per unit endosomal space for tissue and brain
k_{deg}	1/h	First order degradation rate constant of FcRn unbound mAb within the endosomal space

References

1. Pardridge WM (2016) CSF, blood–brain barrier, and brain drug delivery. Expert Opin Drug Deliv 13:963–975
2. Neves V, Aires-da-Silva F, Corte-Real S, Castanho MARB (2016) Antibody approaches to treat brain diseases. Trends Biotechnol 34:36–48
3. Dostalek M, Gardner I, Gurbaxani BM, Rose RH, Chetty M (2013) Pharmacokinetics, pharmacodynamics and physiologically-based pharmacokinetic modelling of monoclonal antibodies. Clin Pharmacokinet 52:83–124
4. Matsuo E, Shin R, Billingsley M, Devoorde A, Oconnor M, Trojanowski J, Lee V (1994) Biopsy-derived adult human brain tau is phosphorylated at many of the same sites as Alzheimers disease paired helical filament tau. Neuron 13:989–1002
5. Hillered L, Vespa P, Hovda D (2005) Translational neurochemical research in acute human brain injury: the current status and potential future for cerebral microdialysis. J Neurotrauma 22:3–41
6. Pestalozzi BC, Brignoli S (2000) Trastuzumab in CSF. J Clin Oncol 18:2349–2351
7. Stemmler H, Schmitt M, Willems A, Bernhard H, Harbeck N, Heinemann V (2007) Ratio of trastuzumab levels in serum and cerebrospinal fluid is altered in HER2-positive breast cancer patients with brain metastases and impairment of blood–brain barrier. Anticancer Drugs 18:23–28
8. Rubenstein J, Fridlyand J, Abrey L, Shen A, Karch J, Wang E (2007) Phase I study of intraventricular administration of rituximab in patients with recurrent CNS and intraocular lymphoma. J Clin Oncol 25:1350–1356
9. Nau R, Sorgel F, Eiffert H (2010) Penetration of drugs through the blood–cerebrospinal fluid/blood–brain barrier for treatment of central nervous system infections. Clin Microbiol Rev 23:858–883
10. Martín-garcía E, Mannara F, Gutiérrez-cuesta J, Sabater L, Dalmau J, Maldonado R, Graus F (2013) Intrathecal injection of P/Q type voltage-gated calcium channel antibodies from paraneoplastic cerebellar degeneration cause ataxia in mice. J Neuroimmunol 261:53–59
11. Wolak DJ, Pizzo ME, and Thorne RG (2015) Probing the extracellular diffusion of antibodies in brain using in vivo integrative optical imaging and ex vivo fluorescence imaging. J Control Release. Elsevier B.V.; 197:78–86.
12. Yadav DB, Maloney JA, Wildsmith KR, Fuji RN, Meilandt WJ, Solanoy H, Lu Y, Peng K, Wilson B, Chan P, Gadkar K, Kosky A, Goo M, Daugherty A, Couch JA, Keene T, Hayes K, Nikolas

LJ, Lane D, Switzer R, Adams E, Watts RJ, Levie KS, Prabhu S, Shafer L, Thakker DR, Hildebrand K, Atwal JK (2017) Widespread brain distribution and activity following anti-BACE1 intracerebroventricular infusion in nonhuman primates. Br J Pharmacol 174:4173–4185
13. Chang H-Y, Morrow K, Bonacquisti E, Zhang WY, Shah DK (2018) Antibody pharmacokinetics in rat brain determined using microdialysis. MAbs 10:843–853
14. Gadkar K, Yadav DB, Zuchero JY, Couch JA, Kanodia J, Kenrick MK, Atwal JK, Dennis MS, Prabhu S, Watts RJ, Joseph SB, Ramanujan S (2016) Mathematical PKPD and safety model of bispecific TfR/BACE1 antibodies for the optimization of antibody uptake in brain. Eur J Pharm Biopharm 101:53–61
15. Kanodia J, Gadkar K, Bumbaca D, Zhang Y, Tong R, Luk W, Hoyte K, Lu Y, Wildsmith K, Couch J, Watts R, Dennis M, Ernst J, Scearce-Levie K, Atwal J, Ramanujan S, Joseph S (2016) Prospective design of anti-transferrin receptor bispecific antibodies for optimal delivery into the human brain. CPT Pharmacometrics Syst Pharmacol 5:283–291
16. Paris-robidas S, Emond V, Tremblay C, Soulet D (2011) In vivo labeling of brain capillary endothelial cells after intravenous injection of monoclonal antibodies targeting the transferrin receptor. Mol Pharmacol 80:32–39
17. Yu YJ, Zhang Y, Kenrick M, Hoyte K, Luk W, Lu Y, Atwal J, Elliott JM, Prabhu S, Watts RJ, and Dennis MS (2011) Boosting brain uptake of a therapeutic antibody by reducing its affinity for a transcytosis target. Sci Transl Med 3:84ra44–84ra44.
18. Moos T, Morgan EH (2001) Restricted transport of anti-transferrin receptor antibody (OX26) through the blood–brain barrier in the rat. J Neurochem 79:119–129
19. Pardaidge WM, Buciak JL, Friden PM (1991) Selective transport of an anti-transferrin through the blood–brain barrier in vivo receptor antibody. J Pharmacol Exp Ther 259:66–70
20. Bien-ly N, Yu YJ, Bumbaca D, Elstrott J, Boswell CA, Zhang Y, Luk W, Lu Y, Dennis MS, Weimer RM, Chung I, Watts RJ (2014) Transferrin receptor (TfR) trafficking determines brain uptake of Tf R antibody affinity variants. J Exp Med 211:233–244
21. Covell DG, Barbet J, Holton OD, Black CDV, Parker RJ, Weinstein JN (1986) Pharmacokinetics of monoclonal immunoglobulin G1, F(ab')2 and Fab' in mice. Cancer Res 46:3969–3978
22. Mackensen DG, Jain RK (1994) Physiologically based pharmacokinetic model for specific and nonspecific monoclonal antibodies and fragments in normal tissues and human tumor xenografts in nude mice. Cancer Res 54:1517–1528
23. Baxter LT, Zhu H, Jain RK, Zhu H, Mackensen DG, Butler WF (1995) Biodistribution of monoclonal antibodies: scale-up from mouse to human using a physiologically based pharmacokinetic model. Cancer Res 55:4611–4622
24. Ferl GZ, Wu AM, DiStefano JJ (2005) A predictive model of therapeutic monoclonal antibody dynamics and regulation by the neonatal Fc receptor (FcRn). Ann Biomed Eng 33:1640–1652
25. Garg A, Balthasar JP (2007) Physiologically-based pharmacokinetic (PBPK) model to predict IgG tissue kinetics in wild-type and FcRn-knockout mice. J Pharmacokinet Pharmacodyn 34:687–709
26. Cao Y, Jusko WJ (2012) Applications of minimal physiologically-based pharmacokinetic models. J Pharmacokinet Pharmacodyn 39:711–723
27. Shah DK, Betts AM (2012) Towards a platform PBPK model to characterize the plasma and tissue disposition of monoclonal antibodies in preclinical species and human. J Pharmacokinet Pharmacodyn 39:67–86
28. Cao Y, Balthasar JP, Jusko WJ (2013) Second-generation minimal physiologically-based pharmacokinetic model for monoclonal antibodies. J Pharmacokinet Pharmacodyn 40:597–607
29. Glassman PM, Balthasar JP (2017) Physiologically-based modeling to predict the clinical behavior of monoclonal antibodies directed against lymphocyte antigens. MAbs 9:297–306
30. Brinker T, Stopa E, Morrison J, Klinge P (2014) A new look at cerebrospinal fluid movement. Fluids Barriers CNS 11:1–16
31. Plog B, Nedergaard M (2017) The glymphatic system in central nervous system health and disease: past, present, and future. Ann Rev Pathol 13:379–394
32. Hladky SB, Barrand MA (2014) Mechanisms of fluid movement into, through and out of the brain : evaluation of the evidence. Fluids Barriers CNS 11:1–32
33. Abuqayyas L, Balthasar JP (2013) Investigation of the role of FcγR and FcRn in mAb distribution to the brain. Mol Pharm 10:1505–1513
34. Garg A, Balthasar JP (2009) Investigation of the influence of FcRn on the distribution of IgG to the brain. AAPS J 11:553–557
35. Schlachetzki F, Zhu C, Pardridge W (2002) Expression of the neonatal Fc receptor (FcRn) at the blood–brain barrier. J Neurochem 81:203–206
36. Zhang Y, Pardridge WM (2001) Mediated efflux of IgG molecules from brain to blood across the blood–brain barrier. J Neuroimmunol 114:168–172
37. Cooper PR, Ciambrone GJ, Kliwinski CM, Maze E, Johnson L, Li Q, Feng Y, Hornby PJ (2013) Efflux of monoclonal antibodies from rat brain by neonatal Fc receptor, FcRn. Brain Res 1534:13–21
38. Wang Q, Delva L, Weinreb PH, Pepinsky RB, Graham D, Veizaj E, Cheung AE, Chen W, Nestorov I, Rohde E, Caputo R, Kuesters GM, Bohnert T, Gan LS (2018) Monoclonal antibody exposure in rat and cynomolgus monkey cerebrospinal fluid following systemic administration. Fluids Barriers CNS 15:1–10
39. Noguchi Y, Kato M, Ozeki K, Ishigai M (2017) Pharmacokinetics of an intracerebroventricularly administered antibody in rats. MAbs 9:1210–1215
40. Bergman I, Burckart GJ, Pohl CR, Venkataramanan R, Barmada MA, Griffin JA, Cheung N-K (1998) Pharmacokinetics of IgG and IgM anti-ganglioside antibodies in rats and monkeys after intrathecal administration. J Pharmacol Exp Ther 284:111–115
41. Atwal JK, Chen Y, Chiu C, Mortensen DL, Meilandt WJ, Liu Y, Heise CE, Hoyte K, Luk W, Lu Y, Peng K, Wu P, Rouge L, Zhang Y, Lazarus RA, Scearce-Levie K, Wang W, Wu Y, Tessier-Lavigne M, Watts RJ.(2011) A therapeutic antibody targeting BACE1 inhibits amyloid-β production in vivo. Sci Transl Med 3(84):84ra43.
42. Braen APJM, Perron J, Tellier P, Catala AR, Kolaitis G, Geng W (2010) A 4-week intrathecal toxicity and pharmacokinetic study with trastuzumab in cynomolgus monkeys. Int J Toxicol 29:259–267
43. Kaschka WP, Theilkaes L, Eickhoff K, Skvaril F (1979) Disproportionate elevation of the immunoglobulin G1 concentration in cerebrospinal fluids of patients with multiple sclerosis. Infect Immun 26:933–941
44. Curtin F, Vidal V, Bernard C, Kromminga A, Lang AB, Porchet H (2016) Serum pharmacokinetics and cerebrospinal fluid concentration analysis of the new IgG4 monoclonal antibody GNbAC1 to treat multiple sclerosis: a phase 1 study. MAbs 8:854–860
45. Borvak J, Richardson J, Medesan C, Antohe F, Radu C, Simionescu M, Ghetie V, Ward E (1998) Functional expression of the MHC class I-related receptor, FcRn, in endothelial cells of mice. Int Immunol 101289–1298(10):1289–1298
46. Cauza K, Hinterhuber G, Dingelmaier-Hovorka R, Brugger K, Klosner G, Horvat R, Wolff K, Foedinger D (2005) Expression of

FcRn, the MHC class I-related receptor for IgG, in human keratinocytes. J Invest Dermatol 124:132–139
47. Blumberg R, Koss T, Story C, Barisani D, Polischuk J, Lipin A, Pablo L, Green R, Simister N (1995) A major histocompatibility complex class I-related Fc receptor for IgG on rat hepatocytes. J Clin Invest 95:2397–2402
48. Cianga P, Cianga C, Cozma L, Ward E, Carasevici E (2003) The MHC class I related Fc receptor, FcRn, is expressed in the epithelial cells of the human mammary gland. Hum Immunol 64:1152–1159
49. Akilesh S, Christianson G, Roopenian D, Shaw A (2007) Neonatal FcR expression in bone marrow-derived cells functions to protect serum IgG from catabolism. J Immunol 179:4580–4588
50. Garg A (2007) Investigation of the role of FcRn in the absorption, distribution, and elimination of monoclonal antibodies, Chap 3. PhD Thesis, Dep Pharm Sci., pp. 71–111.
51. Hladky SB, Barrand MA (2016) Fluid and ion transfer across the blood–brain and blood–cerebrospinal fluid barriers; a comparative account of mechanisms and roles. Fluids Barriers CNS 13:1–69
52. Villasenõr R, Ozmen L, Messaddeq N, Grüninger F, Loetscher H, Keller A, Betsholtz C, Freskgård PO, Collin L (2016) Trafficking of endogenous immunoglobulins by endothelial cells at the blood–brain barrier. Sci Rep 6:1–10
53. Urva SR, Yang VC, Balthasar JP (2010) Physiologically based pharmacokinetic model for T84.66: a monoclonal anti-CEA antibody. J Pharm Sci 99:1582–1600
54. Davson H, and Segal MB (1996) Physiology of the CSF and blood–brain barriers. CRC Press, Boca Raton
55. Pizzo ME, Wolak DJ, Kumar NN, Brunette E, Brunnquell CL, Hannocks MJ, Abbott NJ, Meyerand ME, Sorokin L, Stanimirovic DB, Thorne RG (2018) Intrathecal antibody distribution in the rat brain: surface diffusion, perivascular transport and osmotic enhancement of delivery. J Physiol 596:445–475
56. Sarin H (2012) Physiologic upper limits of pore size of different blood capillary types and another perspective on the dual pore theory of microvascular permeability. J Angiogenes 2:1–19
57. Khot A, Tibbitts J, Rock D, Shah DK (2017) Development of a translational physiologically based pharmacokinetic model for antibody-drug conjugates: a case study with T-DM1. AAPS J 19:1715–1734
58. Sobol IM (2001) Global sensitivity indices for nonlinear mathematical models and their Monte Carlo estimates. Math Comput Simulat 55:271–280
59. Wolburg H, Lippoldt A (2002) Tight junctions of the blood–brain barrier : development, composition and regulation. Vascul Pharmacol 38:323–337
60. Roopenian DC, Akilesh S (2007) FcRn : the neonatal Fc receptor comes of age. Nat Rev Immunol 7:715–725
61. St-Amour I, Pare I, Alata W, Coulombe K, Ringuette-goulet C, Drouin-ouellet J, Vandal M, Soulet D, Bazin R, Calon F (2013) Brain bioavailability of human intravenous immunoglobulin and its transport through the murine blood–brain barrier. J Cereb Blood Flow Metab 33:1983–1992
62. Simon MJ, Iliff JJ (2016) Regulation of cerebrospinal fluid (CSF) flow in neurodegenerative, neurovascular and neuroinflammatory disease. Biochim Biophys Acta 1862:442–451
63. Cserr H (1971) Physiology of choroid plexus. Physiol Rev 51:273–311
64. Damkier H, Brown P, Praetorius J (2013) Cerebrospinal fluid secretion by the choroid plexus. Physiol Rev 93:1847–1892
65. Louveau A, Herz J, Alme MN, Salvador AF, Dong MQ, Viar KE, Herod SG, Knopp J, Setliff JC, Lupi AL, Da Mesquita S, Frost EL, Gaultier A, Harris TH, Cao R, Hu S, Lukens JR, Smirnov I, Overall CC, Oliver G, Kipnis J (2018) CNS lymphatic drainage and neuroinflammation are regulated by meningeal lymphatic vasculature. Nat Neurosci 21:1380–1391
66. Mesquita S Da, Fu Z, and Kipnis J (2018) The meningeal lymphatic system: a new player in neurophysiology. Neuron 100:375–88.
67. Levy G (1994) Pharmacologic target-mediated drug disposition. Clin Pharmacol Ther 56:248–252
68. Deane R, Sagare A, Hamm K, Parisi M, LaRue B, Guo H, Wu Z, Holtzman DM, Zlokovic BV (2005) IgG-assisted age-dependent clearance of Alzheimer's amyloid peptide by the blood–brain barrier neonatal Fc receptor. J Neurosci 25:11495–11503
69. Bard F, Cannon C, Barbour R, Burke RL, Games D, Grajeda H, Guido T, Hu K, Huang J, Johnson-Wood K, Khan K, Kholodenko D, Lee M, Lieberburg I, Motter R, Nguyen M, Soriano F, Vasquez N, Weiss K, Welch B, Seubert P, Schenk D, Yednock T (2000) Peripherally administered antibodies against amyloid β-peptide enter the central nervous system and reduce pathology in a mouse model of Alzheimer disease. Nat Med 6:916–919
70. Collin L, Bohrmann B, Gopfert U, Oroszlan-szovik K, Ozmen L, Gruninger F (2014) Neuronal uptake of tau/pS422 antibody and reduced progression of tau pathology in a mouse model of Alzheimer's disease. Brain 137:2834–2846
71. Thom George, Burrell M, Haqqani AS, Yogi A, Lessard E, Brunette E, Delaney C, Baumann E, Callaghan D, Rodrigo N, Webster CI, Stanimirovic DB (2018) Enhanced delivery of galanin conjugates to the brain through bioengineering of the anti-transferrin receptor antibody OX26. Mol Pharm 15:1420–1431
72. Yu YJ, Atwal JK, Zhang Y, Tong RK, Wildsmith KR, Tan C, Bien-Ly N, Hersom M, Maloney JA, Meilandt WJ, Bumbaca D, Gadkar K, Hoyte K, Luk W, Lu Y, Ernst JA, Scearce-Levie K, Couch JA, Dennis MS, Watts RJ. (2014) Therapeutic bispecific antibodies cross the blood–brain barrier in nonhuman primates. Sci Transl Med 6:261ra154.
73. Couch JA, Yu YJ, Zhang Y, Tarrant JM, Fuji RN, Meilandt WJ, Solanoy H, Tong RK, Hoyte K, Luk W, Lu Y, Gadkar K, Prabhu S, Ordonia BA, Nguyen Q, Lin Y, Lin Z, Balazs M, Scearce-Levie K, Ernst JA, Dennis MS, Watts RJ. (2013) Addressing safety liabilities of TfR bispecific antibodies that cross the blood–brain barrier. Sci Transl Med 5:183ra57,1–12.
74. Okuyama T, Sakai N, Yamamoto T, Yamaoka M, Tomio T (2018) Novel blood–brain barrier delivery system to treat CNS in MPS II: first clinical trial of anti-transferrin receptor antibody fused enzyme therapy. Mol Genet Metab 123:S109
75. Oshio K, Watanabe H, Song Y, Verkman A, Manley G (2005) Reduced cerebrospinal fluid production and intracranial pressure in mice lacking choroid plexus water channel Aquaporin-1. FASEB J 19:76–78
76. de Lange ECM (2013) Utility of CSF in translational neuroscience. J Pharmacokinet Pharmacodyn 40:315–326
77. Kumar G, Smith Q, Hokari M, Parepally J, Duncan M (2007) Brain uptake, pharmacokinetics, and tissue distribution in the rat of neurotoxic N-butylbenzenesulfonamide. Toxicol Sci 98:607–609
78. Rudick R, Zirretta D, Herndon R (1982) Clearance of albumin from mouse subarachnoid space: a measure of CSF bulk flow. J Neurosci Methods 6:253–259
79. Yamamoto Y, Välitalo PA, Wong YC, Huntjens DR, Proost JH, Vermeulen A, Krauwinkel W, Beukers MW, Kokki H, Kokki M, Danhof M, van Hasselt JGC, de Lange ECM (2018) Prediction of human CNS pharmacokinetics using a physiologically-based pharmacokinetic modeling approach. Eur J Pharm Sci 112:168–179
80. Ridgway J, Turnbull L, Smith M (1987) Demonstration of pulsatile cerebrospinal-fluid flow using magnetic resonance phase imaging. Br J Radiol 60:423–427

81. Westerhout J, Ploeger B, Smeets J, Danhof M, de Lange ECM (2012) Physiologically based pharmacokinetic modeling to investigate regional brain distribution kinetics in rats. AAPS J 14:543–553
82. Abbott N (2004) Evidence for bulk flow of brain interstitial fluid: significance for physiology and pathology. Neurochem Int 45:545–552
83. Szentistványi I, Patlak C, Ellis R, Cserr H (1984) Drainage of interstitial fluid from different regions of rat brain. Am J Physiol 246:F835–844
84. Kovačević N, Henderson J, Chan E, Lifshitz N, Bishop J, Evans A, Henkelman R, Chen X (2005) A Three-dimensional MRI Atlas of the Mouse Brain with Estimates of the Average and Variability. Cereb Cortex 15:639–645
85. Yamamoto Y, Välitalo PA, Huntjens DR, Proost JH, Vermeulen A, Krauwinkel W, Beukers MW, Van Den Berg DJ, Hartman R, Wong YC, Danhof M, Van Hasselt JGC, de Lange ECM (2017) Predicting drug concentration-time profiles in multiple CNS compartments using a comprehensive physiologically-based pharmacokinetic model. CPT Pharmacometrics Syst Pharmacol 6:765–777
86. Dorr AE, Lerch JP, Spring S, Kabani N, Henkelman RM (2008) High resolution three-dimensional brain atlas using an average magnetic resonance image of 40 adult C57Bl/6J mice. Neuroimage 42:60–69
87. Strazielle N, Ghersi-Egea JF (2000) Choroid plexus in the central nervous system: biology and physiopathology. J Neuropathol Exp Neurol 59:561–574
88. Johanson CE, Duncan JA, Klinge PM, Brinker T, Stopa EG, Silverberg GD (2008) Multiplicity of cerebrospinal fluid functions: new challenges in health and disease. Cerebrospinal Fluid Res 5:1–32
89. Silverberg G, Heit G, Huhn S, Jaffe R, Chang S, Bronte-Stewart H, Rubenstein E, Possin K, Saul T (2001) The cerebrospinal fluid production rate is reduced in dementia of the Alzheimer's type. Neurology 57:1763–1766